FACULTY OF SCIENCE AND TECHNOLOGY

MASTER'S THESIS

Study programme / specialisation: Marine & Offshore Technology	The *autumn* semester, *2022* Open / ~~Confidential~~
Author: Hans Peter Schmidt	
Supervisor at UiS: Associate Professor Lin Li Co-supervisor: External supervisor(s):	
Thesis title: **Response analysis of an offshore fish farm under combined waves and current**	
Credits (ECTS): 30	
Keywords: Offshore Fish Farm Dynamic Motions Mooring Line Tension Hydrodynamic Loads	Pages: 72 + appendix: 11 Stavanger, *(15.12.2022)*

Hans Peter Schmidt

RESPONSE ANALYSIS OF AN OFFSHORE FISH FARM UNDER COMBINED WAVES & CURRENT

Master of Science Thesis in Marine & Offshore Technology
December 2022
Supervisor: Associate Professor Lin Li

University of Stavanger
Faculty of Science and Technology
Department of Mechanical and Structural Engineering and Material Science

ABSTRACT

Global increasing demand for aquatic foods, limitations of sheltered water locations, and ecological concerns have led a movement towards expanding marine finfish aquaculture to exposed waters in the open ocean. Despite the advantages of offshore fish farming, there are many challenges regarding the harsher environmental conditions in these locations, making it necessary to develop new concepts of fish farms to withstand these conditions. The purpose of this paper is to study a weather vanning module-based fish farm concept for operation in exposed waters. The concept consists of a turret-moored base-module and fish cage modules, where two rows of cage modules are connected to the moored base-module to form an "L" shaped fish farm. The module-based concept and easy connection systems between modules allow the fish farm to be easily arranged with different numbers of cages and only requires one mooring system for the whole fish farm. The hydrodynamic properties of the base-module have been obtained in the frequency-domain using a panel model. The grid-frame of the cage-modules has been modeled using slender cylindrical elements, where the hydrodynamic loads have been formulated using Morison's equation. A simplified model of the nets is created with slender cylindrical elements using the screen model method to formulate equivalent hydrodynamic loads. The mooring lines are modeled as bar elements and the module connectors are modeled as beam elements. The coupled time-domain method was applied to perform sensitivity studies on the number of cage-modules in the fish farm, wave conditions, and current velocities. The responses investigated in detail include the global motion responses of the base-module, tension in the mooring lines, and axial forces in the connectors.

Content

List of figures

List of tables

Chapter One

INTRODUCTION

1.1. Background

As global population and demand for food sources continue to increase, the marine aquaculture industry is looking for sustainable methods of increasing the production of aquatic foods such as salmonid species. According to FAO (2022), the global apparent consumption of aquatic foods has grown at an average annual rate of 3 percent since 1961. The trend for increasing annual growth in demand for aquatic foods is shown in Figure 1.

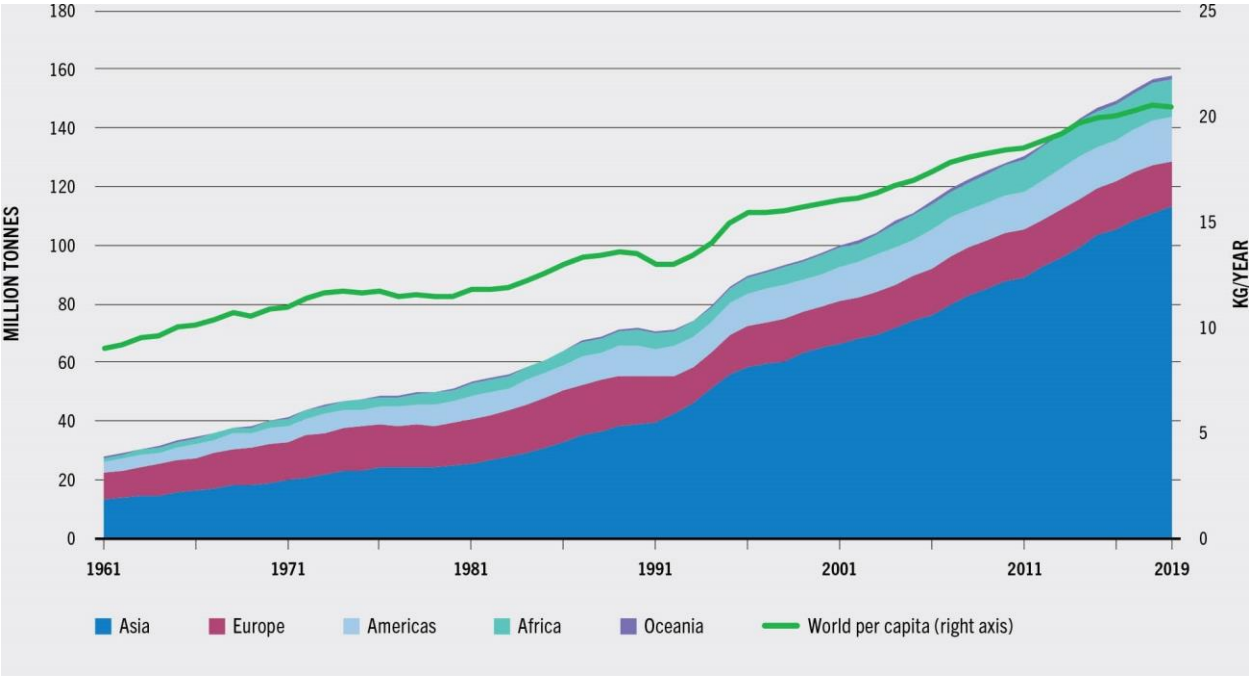

Figure 1. Annual consumption of aquatic food per continent (FAO, 2022).

The conventional form of farming salmonid species has required certain conditions for optimal production, which has limited production to certain regions in the world. These conditions are water temperature, biological conditions, and until recently, sheltered waters. Norway, Chile, Scotland, and Canada have been dominant in the production of farmed salmonids due to having geographical advantages which support the optimal conditions mentioned. The countries previously mentioned count on coastlines with fjords which are described as sea inlets of deep and narrow valleys formed from glacial activity. Examples of fjords located in Chile and Norway are shown in Figure 2.

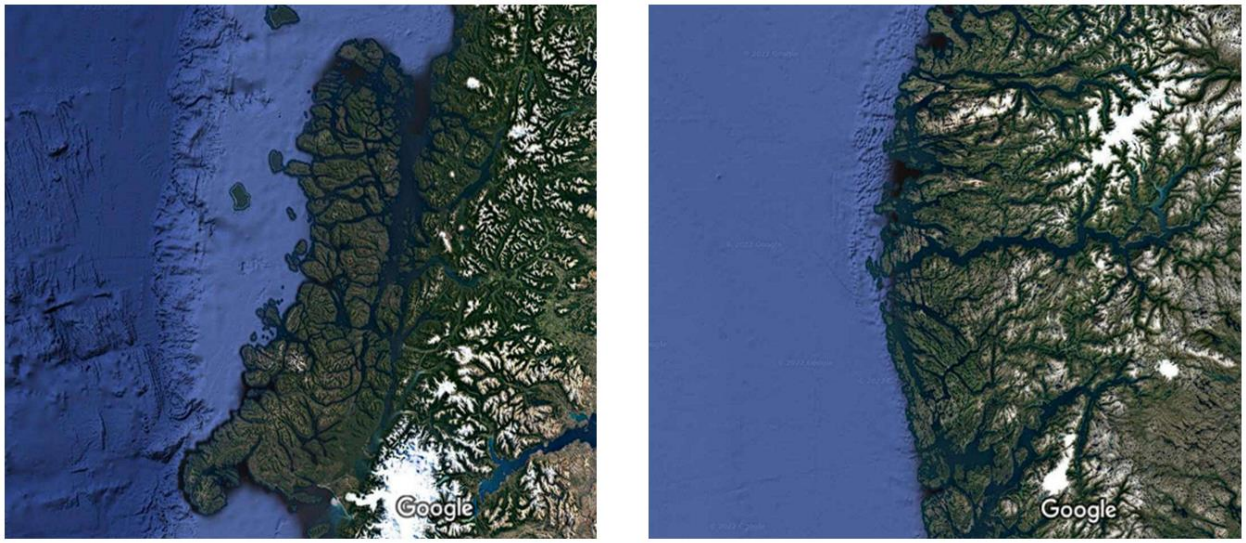

(a) (b)

Figure 2. Fjord regions in (a) Chile and (b) Norway. (Google, n.d.)

Figure 2(a) shows a region in the south of Chile which contains fjords which are inlets of the Pacific Ocean seen on the left. Figure 2(b) shows fjords on the west coast of Norway which are inlets of the North Sea. The availability of sheltered water locations for fish farms is limited worldwide, creating a need for the implementation of offshore fish farming to increase the supply of aquatic foods to keep up with future demand if the trend shown in Figure 1 continues. Additionally, offshore locations offer improved water qualities, less fish density, and reduced chance of infection from diseases, all factors which improve the welfare of farmed fish (DNV, 2021).

1.2. State of the art

Conventional sheltered-water fish farms

Conventional sheltered-water fish farms typically consist of individual or grouped floating-collar net pens. The nets are attached to a moored floating collar and have weights or rigid collar sinkers at the bottom of the nets. Figure 3 shows illustrations of two typical conventional fish farms

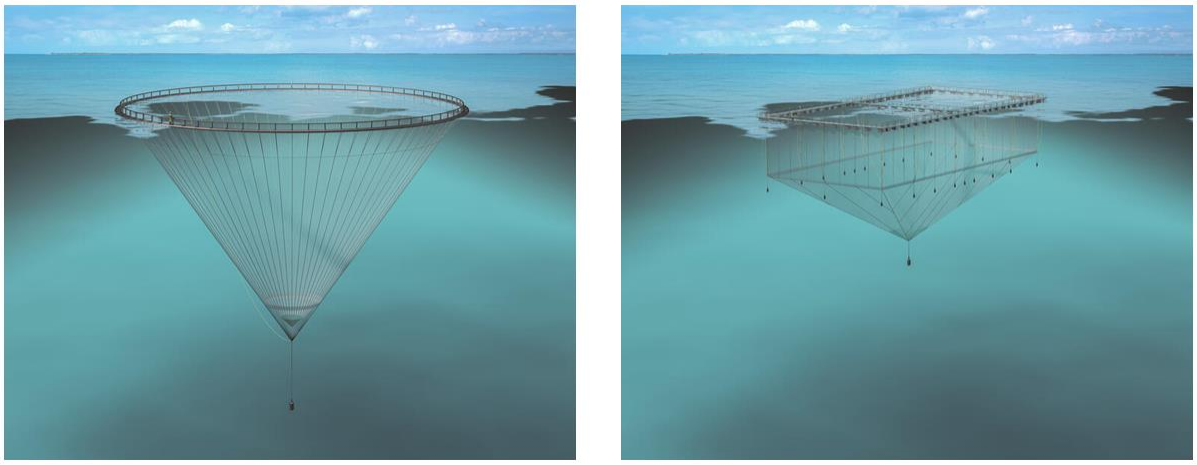

Figure 3. Conventional sheltered-water fish cages. (AKVA GROUP, n.d.)

The illustration of the left of Figure 3 shows a conical shaped cage with a circular floating collar made from high-density polyethylene. The illustration on right shows a rectangular shaped cage with a floating collar comprised of carbon-steel gangways with attached floaters.

In both cases shown in Figure 3 weights are used to try to preserve the shape of the net, yet deformation is still an issue when exposed to high currents (Cheng et al., 2022; Mjåtveit et al., 2022). Furthermore, net deformation reduces the volume inside the net cage and increases stocking density, which negatively affects production and fish welfare (Oppedal et al., 2011). Fish welfare is highly dependent on the internal volume of the net pen and the density of fish in the cage.

Conventional farms typically include a group of fish cages and a feed barge, which is a floating structure that serves mainly as the operational center, storage unit for the fish feed, and distributes the fish feed to the cages. The farms may vary with the shape, size and number of cages, mooring arrangements, and the capacity of the feed barge. An example of a common conventional fish farm arrangement is shown in Figure 4.

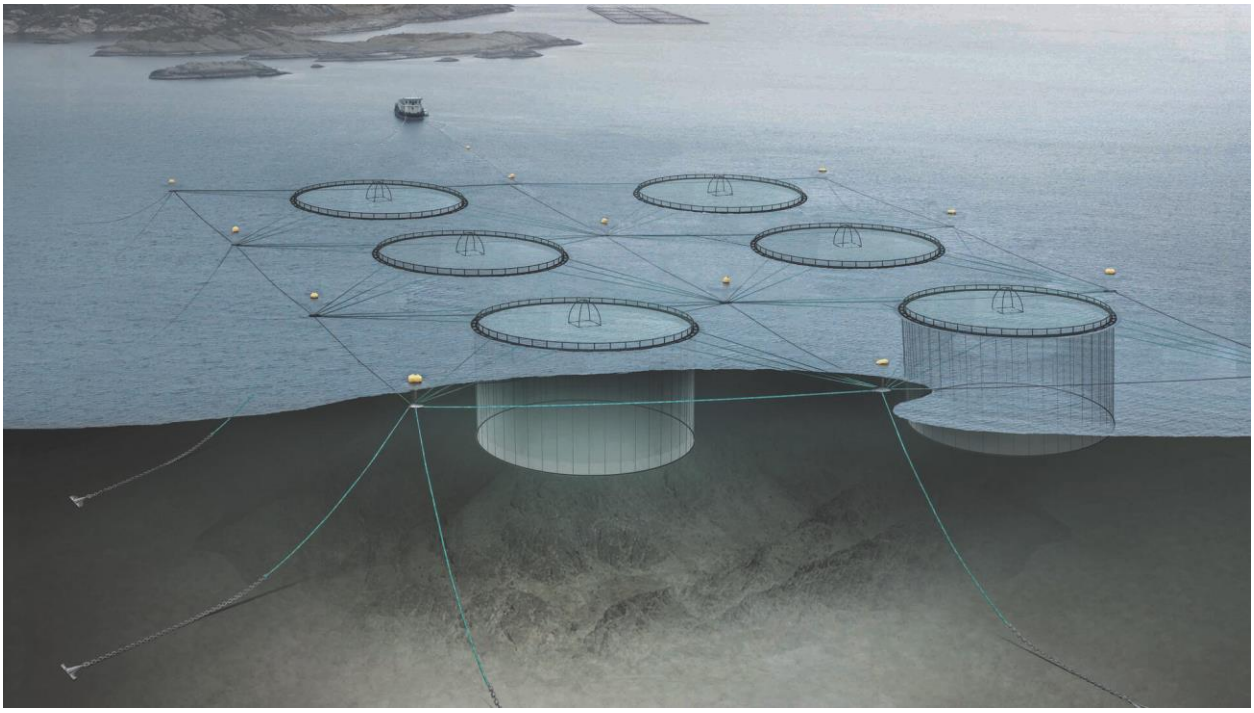

Figure 4. Conventional fish farm arrangement. (AKVA GROUP, n.d.)

The fish farm in Figure 4 shows an arrangement of six circular plastic cages with shared mooring lines and buoys, and a feed barge which feeds the cages via plastic tubes.

An issue with conventional fish farms is the occurrence of fish escaping from cages into the open sea. Large escapement of salmonids from fish farms may occur if there is a failure of the net pen structure, such as the event in 2018 in Chile, where around 900,000 Atlantic salmon escaped (Gomez-Uchida et al., 2018). In this case, the cage structures failed during stormy weather conditions. Such incidents cause harm to the local ecosystems and generate negative economic impacts. To reduce the risk of escapement events, research for conventional fish farms has been performed for improving the numerical modeling of the nets to better estimate the environmental loads acting on the fish farms, see (Cheng et al., 2020). Additionally, research organizations and companies such as SINTEF and Aquastructures AS, have developed analysis tools for modeling and performing simulations of fish farms under the influence of different environmental conditions to study the hydrodynamic and structural responses of fish farms.

Offshore fish farms

The interest in expanding salmonid fish farming to more exposed locations has led to the development and research of new concepts. These new concepts aim to address the challenges caused by the more extreme environmental conditions in exposed locations. Some different concepts which have been developed using proven technology from the oil and gas, maritime, and aquaculture industries are shown in Figure 5.

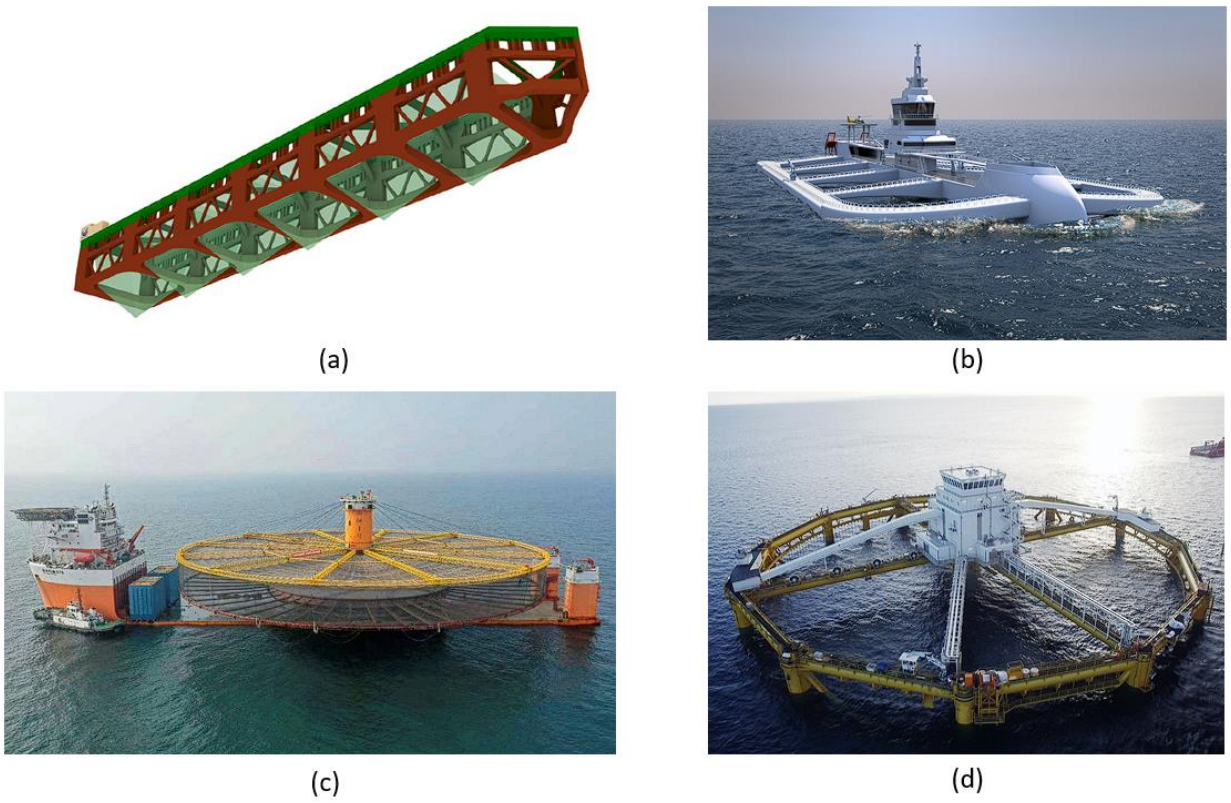

Figure 5. (a) Havfarm 1 (Mobron et al., 2022). (b) Ocean Ark Vessel (RINA, 2021). (c) Semi-submersible Spar Fish Farm (Trauthwein, 2020). (d) Ocean Farm 1 (SalMar ASA, n.d.).

"Havfarm 1", shown in Figure 5(a), is a turret moored vessel shaped fish farm which has the capability to weathervane and is currently in its pilot stage in Norway. Studies have been performed on the global responses in different environmental conditions (Li et al., 2018, 2019), and structural analysis of "Havfarm 1" (Mobron et al., 2022).

Figure 5(b) displays a self-propelled vessel-shaped concept which has been approved by ship classification society RINA (RINA, 2021). The incorporated propulsion allows the fish farm to easily avoid storms, algae blooms, and heatwaves.

A semi-submersible spar concept is shown in Figure 5(c). This concept has been in operation off the coast of China and consists of a circular cage with a spar type floater and has the capability to control its draft with ballast water. This function allows the cage to be submerged to a depth where there is reduced exposure to wave forces in stormy conditions (Trauthwein, 2020). Maintenance tasks can also be performed by reducing ballast and emerging the cage above the still waterline.

Another circular shaped fish farm, named “Ocean Farm 1”, is shown in Figure 5(d). This concept is a pioneer semi-submersible fish farm that has been operating since 2017 and has completed two production cycles in exposed locations. Positive results in the production of salmon have been published by the officials. Due to the success of “Ocean Farm 1”, SalMar and its partnering companies are developing two similar projects named “Ocean Farm 2” and “Smart Fish Farm” (SalMar ASA, 2022). As a pioneer aquaculture facility operating offshore, “Ocean Farm 1” has become the study object of academic research. Model testing and numerical analysis have been performed for “Ocean Farm 1” (Jin et al., 2021) and for a similar semi-submersible fish farm “Deep Blue 1” (Miao et al., 2021). These studies focused on validating the methods applied in the numerical modelling for these concepts by performing model testing and comparing the results of the calculated and experimental motion responses.

The four concepts described from Figure 5 have the feed barge incorporated into the structures. A concept which comprises of separate cage structures and feed barge has been developed to operate in the arctic region in Norway. The cages have been developed by Norway Royal Salmon and Aker Solutions along with their suppliers. Akva Group designed and delivered a robust feed barge able to withstand the extreme conditions of the exposed location for this offshore fish farm. The cage structure and the feed barge are shown in Figure 6.

(a)

(b)

Figure 6. (a) Arctic Offshore Farming cage (Aker Solutions, 2020) and (b) AC800PVDB feed barge (Time, n.d.).

The cage structure and feed barge shown in Figure 6 are designed to withstand conditions of 6.5m significant wave height (Arctic Offshore Farming, n.d.; Time, n.d.). The cage structure is a circular semisubmersible structure with upper and lower pontoons which has a flexible net suspended from the lower pontoon. Figure 6(b), shows the cage in its dry condition, but for operating conditions, the ballast tanks will be filled, causing the structure to submerge to the point where the upper pontoon is at the still waterline.

1.3. Scope and objective

There are a variety of different concepts for offshore fish farming in pilot and developmental phases, but few relevant studies are available. This indicates that there is demand for research and concept development to obtain conventional methods for offshore fish farming. A practical design must compromise between cost effectiveness and resistance to risks pertaining to health, safety, and the environment (HSE). A module-based fish farm, which is described in detail in Chapter 2 has been conceptualized and this study has been developed to evaluate the feasibility of this concept based on the mentioned requirements for a practical design.

From the perspective of structural safety, this study evaluates the feasibility of the module-based offshore fish farm concept using numerical methods to analyze the mooring line tension, global motions, and local forces in the module connectors in relevant environmental conditions.

Coupled time-domain analyses are performed on models like the one shown in Figure 7 using the state-of-the-art tool SIMO-RIFLEX. This tool simulates the responses of the system caused by loads induced from different wave and current conditions. Studying the motions of the fish farm is important for understanding the dynamic loads on the mooring lines and rigid connectors. It also gives insights on how to improve the workability onboard the fish farm. The mooring line tension analysis provides an indication on how to re-dimension the mooring lines to reduce costs and improve operational safety. The local force analysis of the connectors instructs the design of connectors to reduce risk of failures in the cages.

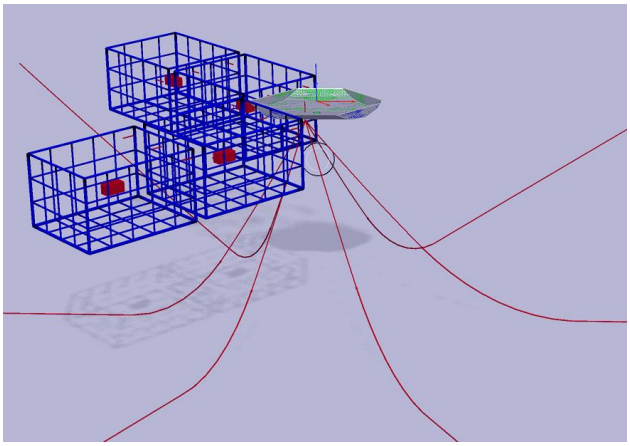

Figure 7. Numerical model of the module-based offshore fish farm with four cages.

Chapter Two

MODULE-BASED OFFSHORE FISH FARM CONCEPT

2.1. Description of concept

The Module-based Offshore Fish Farm concept consists of a single-point turret-moored base-module and individual rigid-frame cage-modules with nets. Two cage-modules can be directly connected to the base-module and additional cage-modules can then be connected to those modules, forming two rows of cages in a 90 degree "L" configuration. A general arrangement of the Module-based Offshore Fish Farm concept is illustrated in Figure 8.

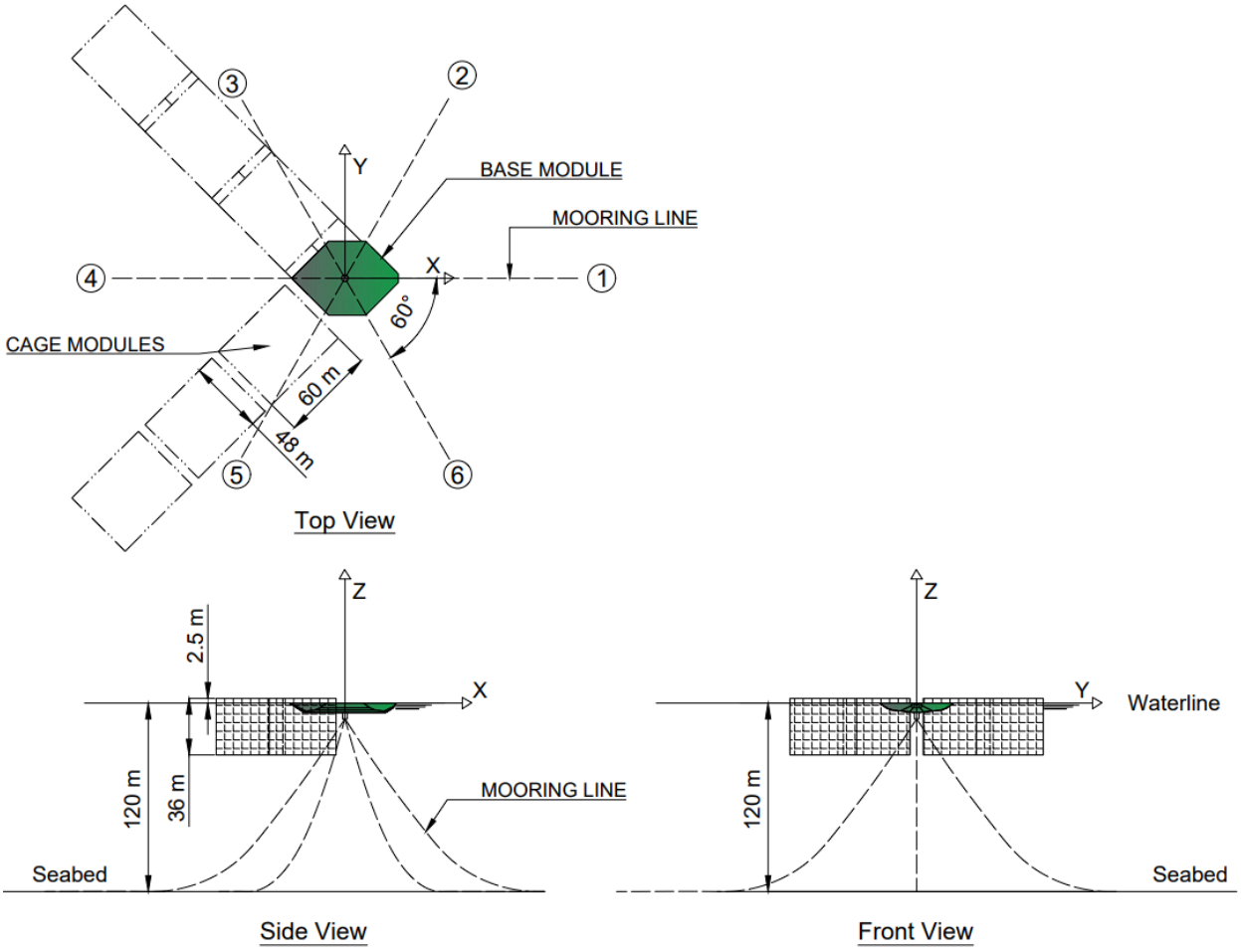

Figure 8. General arrangement of the module-based offshore fish farm. Top view: 6 Cages. Side and front views: 2 Cages.

The configuration of the number of cages in each row would be specific to the production needs of the site and can be easily modified by simply connecting or disconnecting the modules. The easy connection mechanism between modules provides advantages for performing maintenance on individual cages. It also enables relocation in case of storms. In addition, isolating a cage can

prevent the further spread of parasites or disease. The “V” or “L” configuration of the fish cages, as shown in the “top view” in Figure 8, and the ability to weathervane, allow each cage to have direct exposure to the ocean current, providing a more balanced condition in all cages. Nets introduce a wake effect and reduce the flow velocity of the water (Bi et al., 2013), therefore, the “L” shape configuration of the modules is optimal for water exchange in all cages. Asymmetric configuration such as the ones shown in Figure 9 are also possible, but the analysis of dynamic responses for such scenarios is beyond the scope of this study.

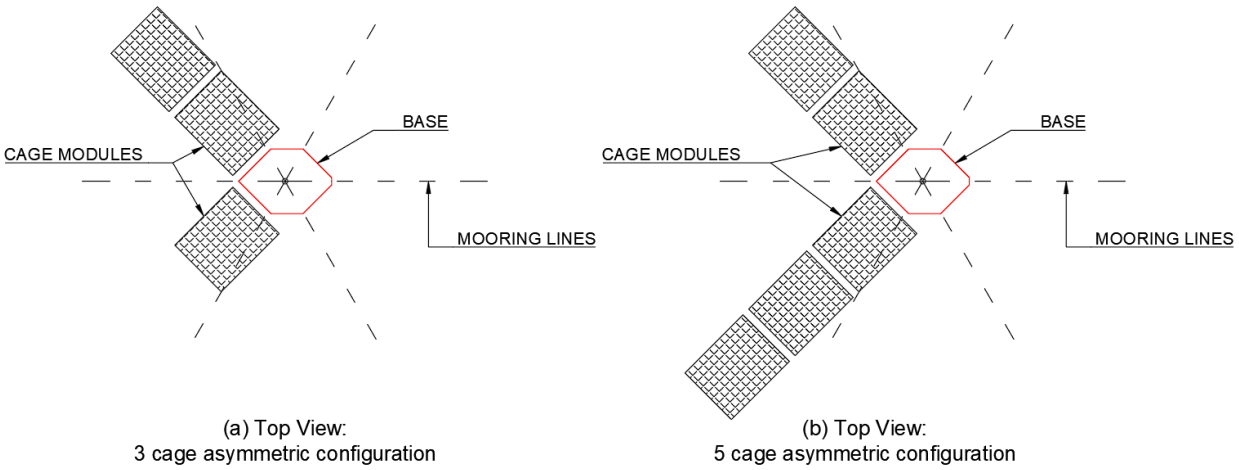

Figure 9. Asymmetric configurations with (a) 3 cages and (b) 5 cages.

2.2.Base-module

The base-module fulfills the function of a feed barge and as the mooring point for the whole fish farm. As shown in Figure 10, the base-module is a ship-shaped barge with a bow, stern, and a rounded midship section.

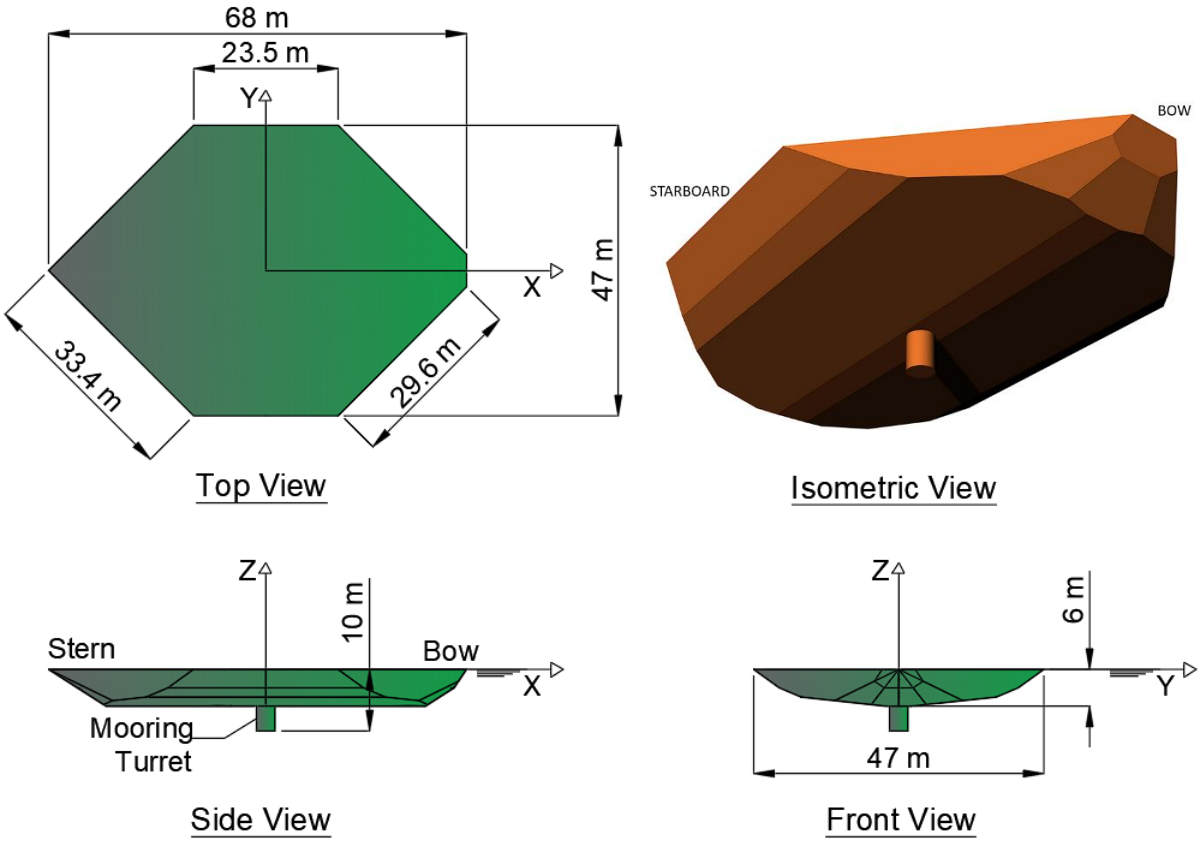

Figure 10. Base-module dimensions.

During operation, the base-module will have different loading conditions due to varying amounts of fish-feed in storage, supplies and other factors, which affect the weight and center of gravity, causing changes in the draft, trim, and heel. This study is limited to one loading condition, for which the principal dimensions are presented in Table 1.

Table 1. Principal dimensions of the base-module

Principal Dimensions	
Length (m)	68
Breadth (m)	47.2
Draft to keel (m)	6
Displacement weight (ton)	10662
Submerged volume (m3)	10402

For comparison, the model AC800PVDB feed barge for exposed locations shown in Figure 6(b) is 64.8 meters long, 12 meters wide, and has a feed storage capacity of 800 metric tons (Time, n.d.). The base-module has a similar length but is almost four times the wider, suggesting that it may store a lot more than 800 metric tons. The larger feed and supply storage capacity of the base-module provides advantages in the logistics as it will reduce the number of trips supply vessels will need to make to the farming location, effectively reducing costs and fuel consumption, along with increasing sustainability. Considerations can also be made for including capabilities for processing the salmon that has reached the end of its cycle, eliminating the need for the transport of live salmon via wellboats to on land processing plants.

2.3. Cage-module

The cage-modules shown in Figure 11 consist of grid-like panels with tubes spaced six meters apart and hollow spherical joints at the intersections between tubes. The cages are 60 meters long, 48 meters wide, and 36 meters tall. Each cage-module has an approximate volume of 100,000 m3, whereas “Ocean Farm 1” has a total net volume of 250,000 m3 and “Havfarm 1” has a total net volume of 414,000 m3.

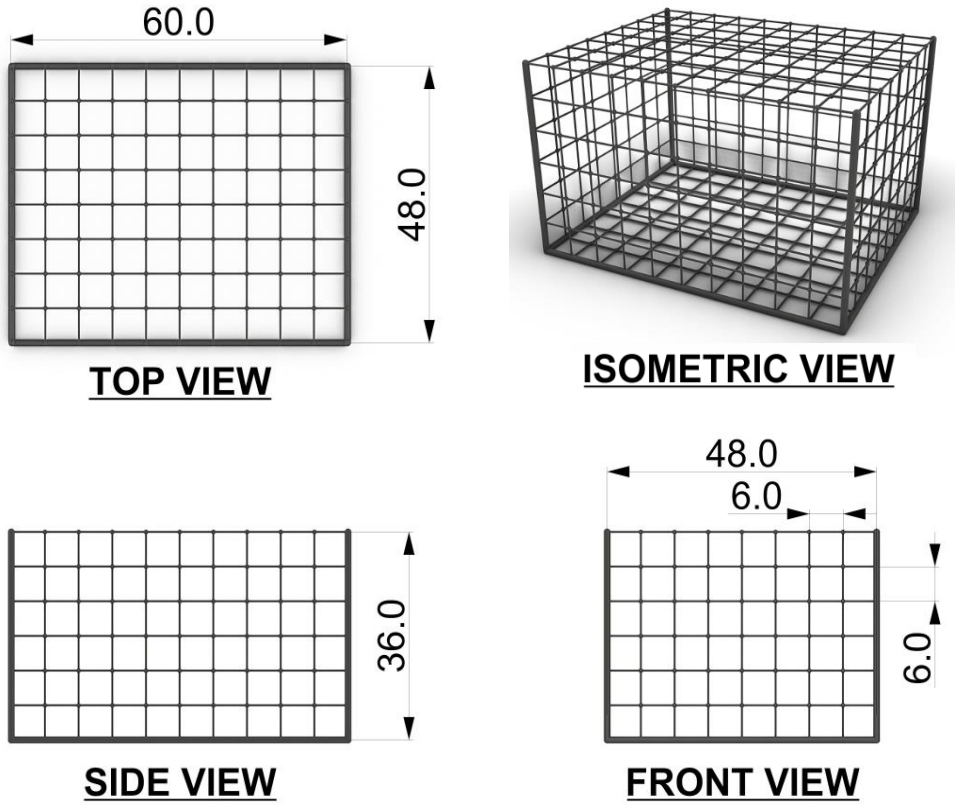

Figure 11. Top, side, front and isometric views of the cage-module frame.

A previous study focused on structural analysis of the cage-module presented by Sun et al. (2022) shows that the design of the truss-type offshore cage meets the requirements for the yield strength for 6-meter wave heights.

The truss-type offshore cage provides many points for fastening fish farming nets on its rigid structure, minimizing the effects of net deformation and reduced cultivation volume caused by high flow velocities.

2.4. Turret and mooring system.

The mooring system consists of six spread catenary mooring lines connected to an internal mooring turret on the base-module. A mooring turret is a device which provides a single-point connection between a floater and multiple mooring lines which allows the floater to passively revolve about its Z-axis. The ability to weathervane reduces the loads within the fish farm and increases the spread area of the waste on the seabed. The components of the mooring lines and their properties are presented in Table 2.

Table 2. Mooring line components

Description	Nominal Diameter (mm)	Segment Length (m)	Submerged Weight (kN/m)	Breaking Strength (kN)
Anchor	-	-	-	-
Chain	165	530	4.644	18699
Link	-	1	20	-
Wire rope	135	90	0.744	18943
Link	-	1	20	-
Fairlead	-	-	-	-

Each mooring line consists of a combination of chain and wire rope, where the chain section is linked to the anchor and the wire rope is linked to the chain and to the turret. Steel wire rope has been selected for the portion of the mooring line that is connected to the turret to reduce the risk of the mooring lines causing rips in the cage nets if contact occurs.

Chapter Three

THEORETICAL BACKGROUND

To advance the design of the module-based offshore fish farm it is necessary to understand how this floating structure will respond in its intended environment. A moored floating structure experiences loads from waves and current which cause responses in the motions and internal forces of the structure. This section explains the theory behind waves, excitation loads caused by waves and currents acting on different elements of the fish farm, and motions of floating bodies.

3.1. Linear waves

In large bodies of water, waves are a naturally occurring phenomena which may be caused by wind, tides, movements of floating structures, earthquakes, and landslides. Waves at a location may exist due to local winds or may have been caused by distant storms and travelled large distances across the body of water. To approximate the behavior of sea waves, linear wave theory is one method that may be applied. Linear wave theory is derived from potential flow theory, which is used as an approximation to describe the velocity potential of a fluid as a gradient of a scalar function. For this approximation to be possible, the flow is assumed to be homogeneous, incompressible, continuous, and non-viscous. The velocity component in any direction of a point in a fluid can be obtained with the derivative of the velocity potential function with respect to that direction. For example, in a 3-D cartesian coordinate system, the fluid velocities u, v, w, in the x-, y-, and z-directions, respectively, can be calculated as:

$$\mathrm{u} = \frac{\partial \Phi}{\partial x}, \quad v = \frac{\partial \Phi}{\partial y}, \quad w = \frac{\partial \Phi}{\partial z} \tag{3.1}$$

To satisfy the potential flow theory, the continuity equation, which is derived from the principle of conservation of mass, is applied on the velocity potential to obtain the Laplace equation for incompressible fluids:

$$\nabla^2 \Phi = \frac{\partial^2 \Phi}{\partial x^2} + \frac{\partial^2 \Phi}{\partial y^2} + \frac{\partial^2 \Phi}{\partial z^2} = 0 \tag{3.2}$$

The velocity potential of a fluid must also be irrotational, therefore, the following conditions for the velocity potential must be satisfied:

$$\frac{\partial v}{\partial x} - \frac{\partial u}{\partial y} = 0 \qquad \frac{\partial w}{\partial y} - \frac{\partial v}{\partial z} = 0 \qquad \frac{\partial u}{\partial z} - \frac{\partial w}{\partial x} = 0 \tag{3.3}$$

(x,y) plane (y,z) plane (x,z) plane

The basics of potential flow theory can be applied to harmonic waves to obtain a wave velocity potential. To satisfy the potential flow theory when applied to waves it must be assumed that the wave steepness is small. Additionally, it must be assumed that the accelerations, velocities, displacements of water particles, and the harmonic pressure have a linear relationship with the wave surface elevation.

A harmonic wave can be represented as sinusoidal wave, therefore, the wave velocity potential with respect to the direction of propagation, x, the vertical distance below the still waterline, z, and time, t, can be initially expressed as a differential equal as:

$$\Phi_w(x,z,t) = P(z) * \sin(kx - \omega t) \tag{3.4}$$

Where, $P(z)$ is an unknown function of the vertical distance below the water level, z. To derive an expression for the wave velocity potential with respect to the distance below the still water line, boundary conditions are applied to equation (3.4). The boundary conditions applied in potential wave theory include the continuity condition, seabed boundary, free surface dynamic boundary, and free surface kinematic boundary.

Continuity condition:

As described in chapter 3.1, the fluid is assumed to be incompressible, meaning that the wave velocity potential must satisfy the continuity condition and the Laplace equation as presented in equation (3.2). This condition is applied to equation (3.4), along with the assumption that the fluid particles only move in the x-z plane for a two-dimensional scenario, yielding a solution for $P(z)$ as:

$$P(z) = (C_1 e^{+kz} + C_2 e^{-kz}) \tag{3.5}$$

In equation (3.5), $C_1$and C_2 are unknown constants, therefore additional boundary conditions must be applied to find an expression for $P(z)$ with known terms.

Seabed boundary condition:

Due to the no-slip condition for fluids, the vertical velocity, w, of the fluid is assumed to be zero at the seabed, where $z = -h$ as is shown in Figure 12.

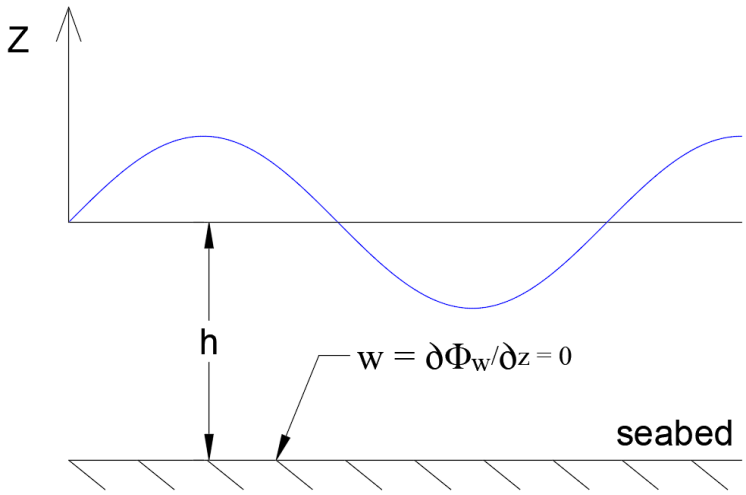

Figure 12. Seabed boundary condition.

Equating the expression for the vertical velocity in equation (3.1) to zero and substituting into the wave velocity potential equation yields the following expression for $P(z)$:

$$P(z) = C * \cosh k(h + z) \tag{3.6}$$

$P(z)$ is now has an unknown constant, C, and is a function of the water depth, h, and vertical distance below the still water level, z.

Free surface dynamic boundary condition:

The free surface dynamic boundary condition states that at the free surface of the fluid, where $z = \zeta$, the pressure is equal to the atmospheric pressure as shown in Figure 13.

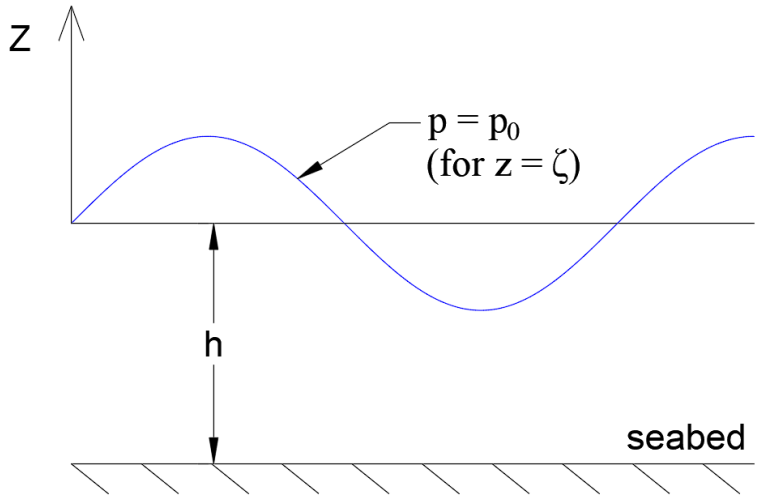

Figure 13. Free surface boundary condition.

This boundary condition is applied to the Bernoulli equation for irrotational and non-stationary flow, which is expressed in terms of the wave velocity potential as:

$$\frac{\partial \Phi_w}{\partial t} + \frac{1}{2}(u^2 + v^2 + w^2) + \frac{p}{\rho} + gz = C^* \tag{3.7}$$

Where, ρ, is the density of the fluid, $p = p_0$, and $z = \zeta$. Taking into consideration the velocity in the y-direction is zero, the u^2 and w^2 terms are small due to the small wave steepness of harmonic waves, disregarding $\frac{p}{\rho}$ and constant, C^*, due to having negligible influence on the wave potential, and expanding the wave potential in a Taylor series, (3.7) is simplified to a linearized expression as:

$$\frac{\partial \Phi_w}{\partial t} + g\zeta = 0 \quad \text{for } z = 0 \tag{3.8}$$

Combining (3.4), (3.6), and (3.8) yields an expression for the wave velocity potential as:

$$\Phi_w = \frac{\zeta_a g}{\omega} * \frac{\cosh k(h+z)}{\cosh hk} * \sin(kx - \omega t) \tag{3.9}$$

Free surface kinematic boundary condition:

The vertical velocity of water particles at the free surface is the same as the vertical velocity of the free surface due to the no-leak condition and is expressed as:

$$\frac{\partial \Phi_w}{\partial z} = \frac{\partial \zeta}{\partial t} \quad \text{for } z = \zeta \tag{3.10}$$

Since this condition is also valid when $z = 0$, equations (3.11)(3.10) and (3.8) are combined to form an expression for the kinematic boundary condition as:

$$\frac{\partial z}{\partial t} + \frac{1}{g} * \frac{\partial^2 \Phi_w}{\partial t^2} = 0 \quad \text{for } z = 0 \tag{3.11}$$

Dispersion relationship

To get a relationship between ω and k, (or T and λ), the expression for the wave velocity potential in (3.9) is substituted into the expression for the kinematic boundary condition in (3.11) to obtain the dispersion relationship for deep water as:

$$\omega = \sqrt{kg} \tag{3.12}$$

$$\lambda = \frac{g}{2\pi} * T^2 \tag{3.13}$$

Water particle kinematics

Using the expressions for the wave velocity potential and the dispersion relationship, the displacements, trajectories, and accelerations of the water particles in the x- and z-directions can be derived.

Regular waves

As a solution of potential wave theory, the wave profile can be expressed as function of t and x as:

$$\zeta = \zeta_a \cos(kx - \omega t) \tag{3.14}$$

Where, the wavelength is expressed as wave number, k, and period is expressed as wave frequency, ω, using:

$$k = \frac{2\pi}{\lambda} \tag{3.15}$$

$$\omega = \frac{2\pi}{T} \tag{3.16}$$

Using (3.14), the wave profile for a regular wave can be described as a time history, or a snapshot as shown in Figure 14.

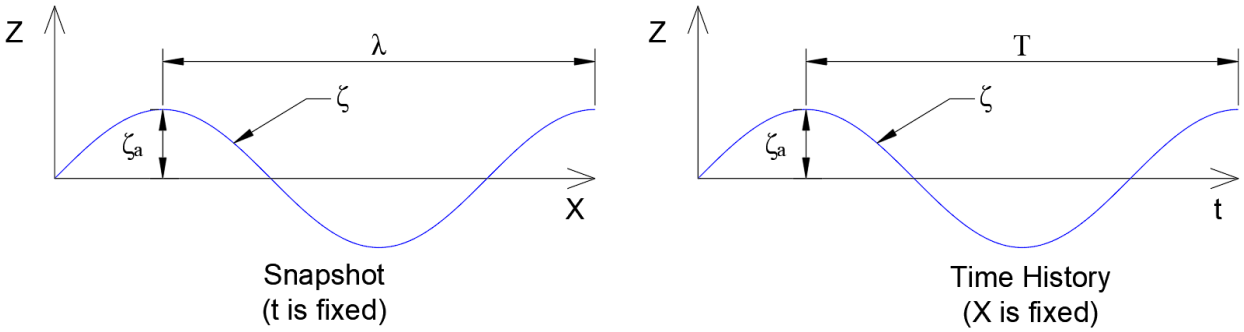

Figure 14. Harmonic wave snapshot (left), and time history (right)

The figure on the left shows a snapshot of a harmonic wave, where the wave profile, ζ, is a function of horizontal distance, x. The figure on the right shows a time history of a harmonic wave, where the wave profile is a function of time, t. The distance between two successive wave crests is the wavelength, λ, and the time between two adjacent wave crests crossing a fixed point is the period, T.

Irregular waves

Naturally occurring waves are usually irregular and are described as a superposition of many regular waves with different phases, amplitudes and periods as shown in Figure 15.

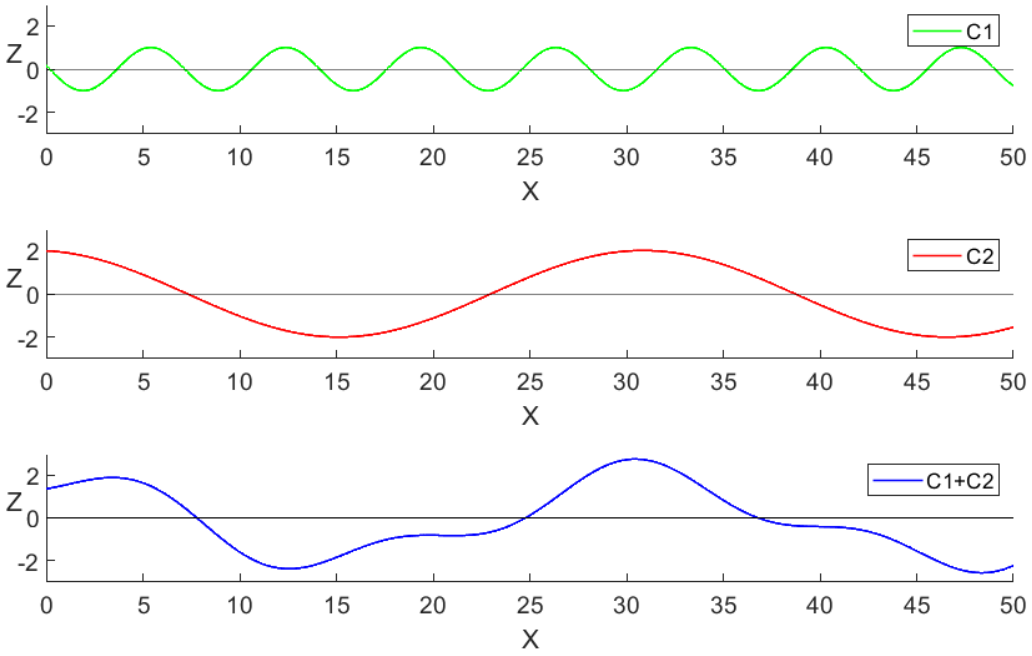

Figure 15. Wave superposition.

As shown in Figure 15, when superimposing two regular waves, C1 and C2, the result is an irregular wave. Irregular sea-states are described by mean wave period, T_p, and the significant wave height, H_s. Significant wave height is the average of the highest one third wave heights. In a 3-hour storm it can be approximated that the largest wave height encountered will be 1.86 times the significant wave height.

A Fourier series analysis is used to study the wave frequencies in an irregular sea state. Through this we obtain a set of values for the wave amplitude, ζ_{a_n}, and frequencies ω_n of the regular waves of which when superimposed, would resemble the irregular sea-state.

A wave energy spectrum is used to describe the distribution of the energy in a sea state with respect to wave frequencies and is expressed as:

$$S_\zeta(\omega_n) * d\omega = \frac{1}{2}{\zeta_{a_n}}^2 \tag{3.17}$$

JONSWAP wave spectra was formulated from measurements of water surface elevations at many locations in the North Sea and describes a not fully developed sea state. The mean JONSWAP wave spectrum is defined as follows:

$$S_\zeta(\omega) = \frac{\alpha g^2}{\omega^5} exp\left(-\beta\left(\frac{\omega_p}{\omega}\right)^4\right) * \gamma^{exp\left(\frac{\left(\frac{\omega}{\omega_p}-1\right)^2}{2\sigma^2}\right)} \quad (3.18)$$

Where, ω_p is the peak frequency, $\omega_p = \frac{2\pi}{T_p}$. β is a form parameter and has a default value of 1.25. σ is a spectral parameter and has default values of 0.07 when $\omega < \omega_p$, and 0.09 when $\omega > \omega_p$. The spectral parameter, α, is defined from the significant wave height, H_s, spectral peak period, T_p, and the peakedness parameter, γ, as:

$$\alpha = 5.061 \frac{{H_s}^2}{{T_p}^4}(1 - 0.287\ln(\gamma)) \quad (3.19)$$

γ is the peakedness parameter where the average value from experimental data is $\gamma = 3.3$. When $\gamma = 3.3$, the mean wave period, T_1, and the zero upcrossing wave period, T_z can be approximated from the peak wave period, T_p, as:

$$T_z = \frac{T_p}{1.2859}, and\ T_1 = 1.0734 T_z \quad (3.20)$$

3.2. Floating rigid body motions

The motions of a floating structure are described in 6 degrees of freedom with three translational and three rotational motions about the origin, which is typically located on the COG of the floater as shown in Figure 16.

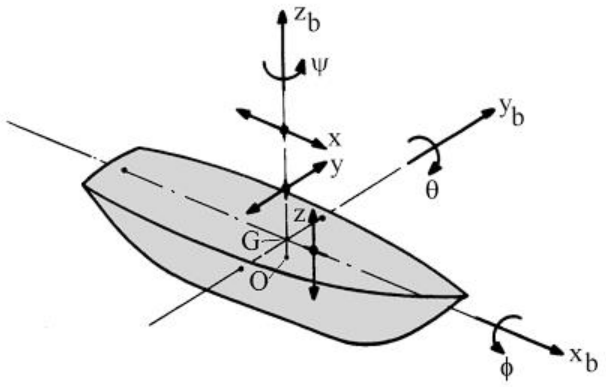

Figure 16. Vessel motions

The translational motions are surge (η_1), sway (η_2), and heave (η_3), which represent the translations in the x-, y-, and z-axis, respectively. The rotational motions are roll $\phi(\eta_4)$, pitch $\Theta(\eta_5)$, and yaw $\psi(\eta_6)$, and their positive directions are shown in Figure 16. When the floaters encounter excitation from harmonic waves, the resulting motions are proportional in amplitude, have the same frequency, and have different phases compared to the exciting wave. The six motions for floating bodies are expressed as:

$$\eta_i(t) = \eta_{ia}\cos(\omega_e t + \varepsilon_{i\zeta}) \tag{3.21}$$

Where, η_{ia} is the motion amplitude, ω_e is the wave frequency, and $\varepsilon_{i\zeta}$ is the phase angle. Using equation (3.21), the expressions for the harmonic velocity and accelerations can be derived and expressed as:

$$\dot{\eta}_i(t) = -\omega_e \eta_{ia} sin(\omega_e t + \varepsilon_{i\zeta}) \tag{3.22}$$

$$\ddot{\eta}_i(t) = -{\omega_e}^2 \eta_{ia} cos(\omega_e t + \varepsilon_{i\zeta}) \tag{3.23}$$

A floater will typically experience a combination of rotational and translational motions. At any point that is not the center of gravity, the rotational motions cause translations in the x-, y-, and z-directions. Therefore, the motions must be superimposed to find these absolute translations. For

small angles of rotation, a transformation matrix is used to find the absolute motions at a given point $P(x_{bP}, y_{bP}, z_{bP})$ of the floater as:

$$\begin{pmatrix} x_P(t) \\ y_P(t) \\ z_P(t) \end{pmatrix} = \begin{pmatrix} x(t) \\ y(t) \\ z(t) \end{pmatrix} + \begin{pmatrix} 0 & -\eta_6(t) & \eta_5(t) \\ \eta_6(t) & 0 & -\eta_4(t) \\ -\eta_5(t) & \eta_4(t) & 0 \end{pmatrix} \cdot \begin{pmatrix} x_{bP} \\ y_{bP} \\ z_{bP} \end{pmatrix} \tag{3.24}$$

The absolute velocity and accelerations at point P, are obtained by expanding ((3.24), substituting the expressions from (3.21), and finding the first and second derivatives with respect to time.

In a linear system, the response amplitude operator (RAO) is used to describe the motion response of a floating rigid body in harmonic waves. RAO is a ratio of the amplitude of the displacement of a motion and the amplitude of the harmonic wave with a certain wave frequency and can be expressed as:

$$\eta_i(\omega) = RAO(\omega) * \zeta(\omega) \tag{3.25}$$

Where $\eta_i(\omega)$ and $\zeta(\omega)$ are the motion response and the wave amplitude for a regular wave as a function of the angular frequency, ω. In the case of irregular sea-states, the response amplitude operator can be expressed as a ratio of the spectral density of the response and the spectral density of the sea-state as:

$$\frac{S_R(\omega)}{S_Z(\omega)} = |RAO(\omega)|^2 \tag{3.26}$$

Where $S(\omega)$ and $S_R(\omega)$ are the wave and response spectrums, respectively.

3.3.Hydrodynamic loads on floating structures

Hydrostatic loads

Buoyancy:

As stated by Archimedes' principle, a floating structure experiences a buoyancy force, F_b, equal to weight of the structure and can be determined by the density of the fluid, ρ, and volume of the fluid which has been displaced by the structure, ∇, as:

$$F_b = \rho g \nabla \tag{3.27}$$

When a floating structure is in equilibrium, the buoyancy force, and the center of gravity of the structure will be vertically aligned. The buoyancy force may also be obtained by integrating the vertical component of the hydrostatic pressure of the fluid acting on the wetted surface of the structure.

Static floating stability:

When an external force that creates moment about the center of gravity of a floating structure is applied, the structure will rotate about its center of gravity. The structure is considered stable if the structure returns to its state of equilibrium when external force is eliminated. The stability of a vessel is typically measured by the metacentric height (GM), which is the distance between the center of gravity of the vessel and the metacenter. The GM has a positive value when the metacenter is above the COG, and negative when below, and for a vessel to be considered stable and return to a state of equilibrium following a disturbance, the GM must be more than zero. The GM of a vessel is typically given as transverse (GM_T) or longitudinal (GM_L) and are expressed as:

$$GM_T = \frac{I_T}{\nabla} + KB - KG \;\; or \;\; GM_L = \frac{I_L}{\nabla} + KB - KG \tag{3.28}$$

Where, I_T and I_L are the second moments of the water plane area about the x-, and y-axis, respectively. KB is the distance between the keel and the center of buoyancy, and KG is the distance between the keel and center of gravity of vessel.

Hydrodynamic loads on large structures

The total force acting on a floating rigid body can be separated into two main components due to the linearity of the motions. The first force component is the hydromechanical force, F_H, that is induced on the body when it is oscillating in undisturbed fluid. The oscillations of the body in a fluid cause radiation of waves away from the body which leads to dissipation of energy from the system. The second force component is the wave force, F_W, induced on the body due to waves acting on a restrained body. Considering these two forces, applying Newton's second law, and treating the floater as a mass-spring system, the equation of motion is expressed as:

$$F_H + F_W = m\ddot{\eta} \tag{3.29}$$

Where F_H is the total reaction force acting on an oscillating body in an undisturbed fluid and is expressed as:

$$F_H = -a\ddot{\eta} - b\dot{\eta} - c\eta \tag{3.30}$$

Combining equations (3.29) and (3.30) and rearranging the terms becomes:

$$F_w = (m + a)\ddot{\eta} + b\dot{\eta} + c\eta \tag{3.31}$$

Where, a is the added mass, b is the damping coefficient, and c is the hydrostatic stiffness. The added mass and damping coefficients can be obtained by performing a forced oscillation test, and the stiffness can be calculated knowing the geometry of the floater and applying Archimedes' principle. The hydrostatic stiffness coefficients only apply to the heave, roll, and pitch motions and are expressed as:

$$\begin{aligned} c_{heave} &= \rho g A_w \\ c_{roll} &= \rho g \nabla G M_T \\ c_{pitch} &= \rho g \nabla G M_L \end{aligned} \tag{3.32}$$

The wave loads, F_w, acting on large structures can be determined by integrating pressure over the body's wetted surface. The pressure is formulated using a combination of the wave potential and the Bernoulli's equation shown in equation (3.7). A new kinematic boundary condition is considered for oscillating floating objects in fluids. This condition states that the velocity of fluid particles at a point at the wetted surface of the body will have the same velocity as the body itself.

Additionally, the radiation condition is also applied, which states that the velocity potential tends to zero as the distance away from the body becomes large. The total force vector in terms of the integrated pressure over the wetted surface using velocity potentials is expressed as:

$$\vec{F} = \rho \iint_S \left(\frac{\partial \Phi_r}{\partial t} + \frac{\partial \Phi_0}{\partial t} + \frac{\partial \Phi_7}{\partial t} + gz \right) \vec{n} \cdot dS \tag{3.33}$$

This expression includes the radiation potential Φ_r for r = 1-6 (each degree of freedom), the undisturbed wave potential Φ_0, and the diffraction potential Φ_7. The force obtained from the undisturbed wave is named the Froude-Krylov force and can also be obtained when performing experimental tests in a wave basin with harmonic waves acting on a restrained body. Since the hull of the floating body is impermeable, waves are diffracted from the surface.

Hydrodynamic loads on slender cylindrical elements

As discussed in chapter 2.3, the structure of the cage-module is made up of cylindrical tubes and spherical joints. This section describes how the hydrodynamic loads acting on these elements are calculated. A cylindrical or spherical element is considered as slender when the diameter is less than 20% of the wavelength (DNV, 2014). Hydrodynamic loads from waves acting on fixed slender elements are described using Morison's equation, which is a combination of inertia and drag forces and is expressed as:

$$F(t) = F_{inertia}(t) + F_{drag}(t) \tag{3.34}$$

The inertia force stems from Newton's second law and linear wave potential theory. Similar to the Froude-Krylov force, the inertia force includes the forces that would be acting on an element in an undisturbed pressure gradient. The inertia force also contains the forces caused by the disturbance that this element has on the pressure gradient as the motion of the fluid creates streamlines around the element. The unit length inertia force in Morisons' equation for a fixed cylindrical element with diameter, D, in waves is expressed as:

$$F_{inertia}(t) = \rho \frac{\pi}{4} C_M D^2 \cdot \dot{u}(t) \tag{3.35}$$

C_M is the inertia coefficient, which is dimensionless and is express as $1 + C_a$, where C_a is the added mass coefficient.

The drag force per unit length in Morison's equation for a cylinder with diameter, D, is derived from real potential flows and constant currents. This force is caused by a disturbance in the flow of the fluid and is expressed for a fixed cylinder as:

$$F_{drag}(t) = \rho \frac{\pi}{2} C_D D \cdot u(t)|u(t)| \tag{3.36}$$

The drag force is proportional to the squared velocity of the fluid and the diameter of the cylinder. Both the dimensionless drag coefficient, C_D, and the added mass coefficient, C_a, are empirical value which are defined by the roughness of the cylinder, the Reynolds number, and the Keulegan-Carpenter number. DNV, 2014 proposes the recommended practices for defining these coefficients.

The previous expressions for the inertia and drag forces consider that the cylinder is fixed. To account for a cylinder that is oscillating in waves, the relative velocities and accelerations of the cylinder with respect to the motions of the fluid particles must be accounted for. Additionally, inertia and drag forces derived from a moving cylinder in still water are superposed to the forces presented in equations (3.35) and (3.36). Applying these considerations, Morison's equation for oscillating cylinders in waves and current can be expressed as:

$$F(t) = \rho \frac{\pi}{4} D^2 \dot{u}_r(t) + \rho \frac{\pi}{4} C_M D^2 \cdot \dot{u}_r(t) + \rho \frac{\pi}{2} C_D D \cdot u_r(t)|u_r(t)| \tag{3.37}$$

Where, $\dot{u}_r$ is the relative acceleration and u_r is the relative velocity.

Hydrodynamic loads on net structure

The nets of a fish farm account for large hydrodynamic loads imposed on conventional fish farms (Gansel et al., 2018). Therefore, it is important to have a precise method for evaluating these hydrodynamic loads. Nets can be described as a collection of slender elements which will experience drag and lift forces and produce turbulent wakes. There are many existing types of fish farm nets which differ in their material composition, netting structures, twine diameters and mesh sizes. For example, Figure 17 shows both knotless and knotted nylon nets with rhombic mesh shapes.

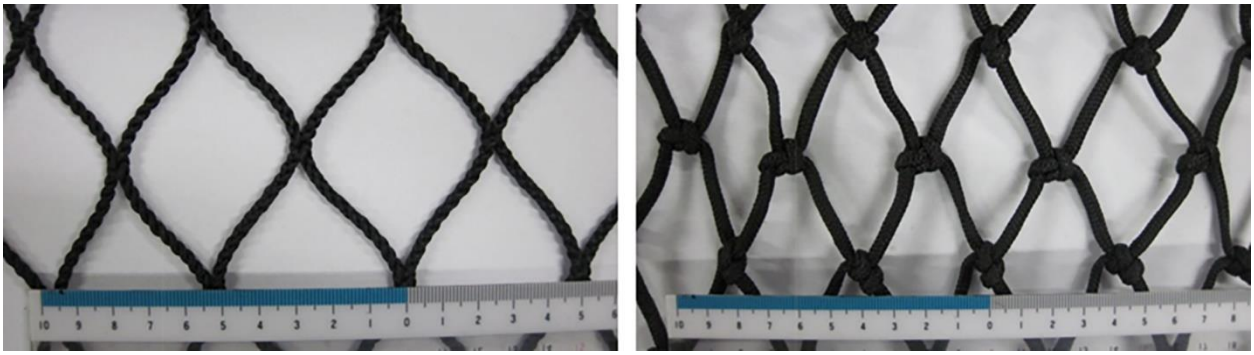

Figure 17. Knotless (left) and knotted (right) nets (Tang et al., 2018).

In the case of mesh structures with knots, such as the net shown in Figure 17(right), the net can be seen as containing cylindrical and spherical elements and Morison's equation can be used to evaluate the loads acting on the nets. In the case of nets, the hydrodynamic loads are dominated by drag forces, therefore, the inertia term in Morison's equation is neglected.

The hydrodynamic loads acting on the nets are dependent on the velocity of the fluid and the hydrodynamic characteristics of the nets. The nets are composed of twines that can be made from different materials with different roughness and twine diameters. Also, the weaving of the fabrics to create the twines, and the way the twines are weaved together to form the net panel can be performed using different methods. Due to these differences, research efforts have been performed to simplify the way to estimate the drag coefficients and drag forces for different types of. A comprehensive and experimental study presented by Cheng et al. (2020) compares calculated drag forces of different Morison and Screen type hydrodynamic models to experimental results of drag force on nets in pure current conditions.

Løland (1991) has presented a way to calculate the hydrodynamic forces on a net using a "screen model" method. This method assumes that the fish nets can be divided into different net panels and the drag and lift coefficients are functions of the solidity ratio of the nets, the Reynolds number, and the angle of attack of the fluid with respect to the net.

The solidity ratio is a function of the mesh size and the thread diameter, which represents the proportion of net threads covering the total area of the net panel (Løland, 1991) and is defined for an ideal knotless net with square mesh as:

$$S_n = \frac{2D}{L} + \frac{1}{2}\left(\frac{D}{L}\right)^2 \tag{3.38}$$

Where, D is the thread diameter, and L is the mesh size as shown in Figure 18.

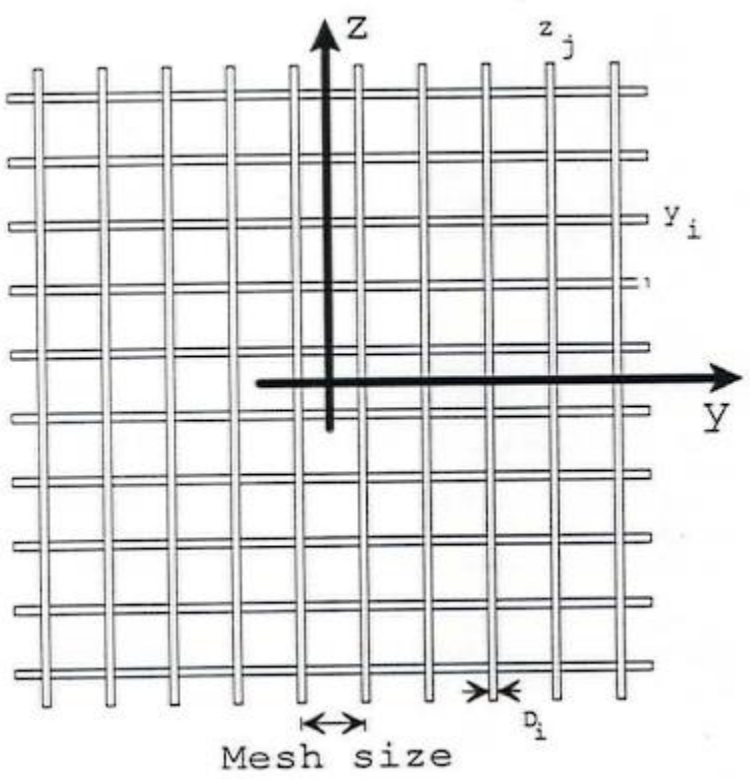

Figure 18. Net dimensions (Løland, 1991).

Empirical formulas for obtaining the drag and lift coefficients as a function of the solidity ratio and the angle of attack have been presented as:

$$C_D(\alpha) = 0.04 + \left(-0.04 + 0.33 * S_n + 6.54 * {S_n}^2 - 4.88 * {S_n}^3\right) * cos\alpha \quad (3.39)$$

$$C_L(\alpha) = \left(-0.05 * S_n + 2.3 * {S_n}^2 - 1.76 * {S_n}^3\right) * sin\alpha \quad (3.40)$$

Using the drag and lift coefficients obtained from (3.39) and (3.40), the drag force, F_D, and the lift force, F_L, are then calculated as:

$$F_D = \frac{1}{2}\rho * C_D(\alpha) * A * U^2 \quad (3.41)$$

$$F_L = \frac{1}{2}\rho * C_L(\alpha) * A * U^2 \quad (3.42)$$

The drag and lift forces on a panel of the net with area, A, are related to the density of the fluid, ρ, the current velocity, U, and the non-dimensional coefficients of drag, C_D, and lift, C_L, for an angle of attack, α, of the current with respect to the net panel.

Chapter Four

NUMERICAL METHODS

4.1. Numerical model of the base-module

The base-module is considered a large volume structure; therefore, its interactions with waves are described with the potential flow theory presented in chapter 3.3. This can be fulfilled by using Sesam package (including GeniE and HydroD). A first order panel model of the base-module has been created using the computer assisted drawing tool GeniE. Subsequently, the panel model is imported into HydroD, where initially the Wadam feature calculates the hydrostatic and inertia properties by integrating the wetted surface of the panel model (Lee, 1995). For this study, the weight distribution has been assumed to be homogeneous, and the center of gravity was assumed to be three meters above the center of buoyancy.

The response amplitude operators (RAO) for the six degrees of freedom of rigid body motions due to incident waves are obtained for different frequencies by solving the equation of motion (Lee, 1995). Selected motion RAO's are presented in Figure 19.

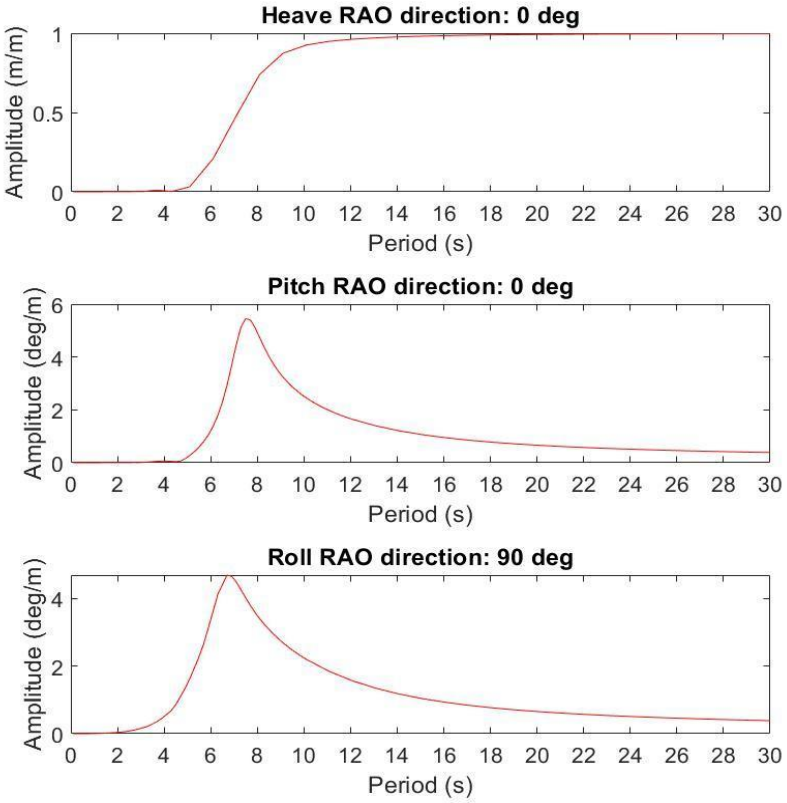

Figure 19. Base-module RAO's for heave, pitch, and roll.

In addition, Wadam applies linear potential theory, integrating the wave loads over the wetted surface of the panel model to calculate the added mass, mean drift forces, first order excitation forces, and potential damping for a given range of frequencies (DNV, 2008). The natural periods for the heave, pitch, and roll motions of the base-module have been calculated to be 7.97, 7.21, and 6.12 seconds, respectively.

4.2. Numerical model of the frame of the cage

Cylindrical slender elements have been used to model the frame. To simplify the numerical model, the spherical joints and the frame tubes are modeled as slender elements with equivalent mass, volume, and hydrodynamic properties. Additionally, the number slender elements in the model have been reduced by increasing the spacing of the tubes from 6 to 12 meters on the grid-like panels of the cage and distributing the volume, mass and hydrodynamic properties of the elements that have been eliminated to the adjacent slender elements.

The inertia and drag forces acting on the equivalent slender elements are formulated based on Morison's equation presented in chapter 0. The inputs for the numerical model are shown in parenthesis in equation (4.1).

$$F = \left(\frac{\pi}{4}\rho C_M D^2\right)\, \dot{u}_{rel} + \left(\frac{1}{2}\rho C_D D\right) * {u_{rel}}^2 \tag{4.1}$$

The non-dimensional drag coefficients, C_D, that have been used for the calculation of the quadratic drag of the tubes and spheres are 1.4 and 0.5, respectively. The non-dimensional added mass coefficient, C_M, for the tubes and spheres are 2.0 and 1.5, respectively.

4.3. Numerical model of the fish nets

Due to the impracticality of the Morison type models, where modeling individual twine elements causes the computational costs to become too large, this study uses a Screen model which has been presented by Løland (1991).

Due to the orientation of the cage-modules, as shown in Figure 8, and the weather-vanning capabilities of the fish farm, the angle of attack of fluid with respected to the nets will typically be 45 degrees. Therefore, the dimensionless drag and lift coefficients for the side panels of net in the cages have been calculated using 45 degrees for α in (3.39) and (3.40). Furthermore, the drag and lift coefficients for the net on the bottom of the cage have been calculated using a 90-degrees angle of attack.

To decrease the computational costs of the time-domain simulations by decreasing the number of slender elements in the model, the quadratic drag and lift forces of the nets are incorporated into the slender elements of the cage frame described in chapter 3.2.

4.4. Numerical model of the mooring lines & module connectors

The mooring lines presented in chapter 2 have been modeled in RIFLEX as flexible elements. RIFLEX uses a nonlinear finite element formulation to perform static analyses, catenary approximations, and nonlinear time domain simulations of the mooring line forces and motions (MARINTEK, 2015) The mooring line elements have been modeled as flexible bars with specified mass, volume, and hydrodynamic properties. The non-dimensional drag and added mass coefficients that have been used to calculate the required inputs for the quadratic drag force coefficients and added mass per unit length can be seen in Table 3.

Table 3. Non-dimensional drag and added mass coefficients

Component	Cdx	Cdy	Cmx	Cmy
Chain	0.20	1.33	0.20	1.00
Cable	0.00	1.20	0.00	1.00

The coefficients shown in Table 3 refer to the drag and added mass in the local x- and y-axes of the elements, where x is tangential, and y is normal to the element.

The module connectors have been modeled as simple beam elements with cross-section properties, stiffness properties for axial, shear, torsion, and bending. and hydrodynamic force coefficients for drag and added mass as presented in Table 4.

Table 4. Connector properties.

Cross-section Properties	Mass Coefficient		(kg/m)	2				
	Ext. Area		(m^2)	0.05				
	Gyration Radius		(m)	0.01				
Stiffness Properties	Bending stiffness		(Nm^2)	1.00E+10				
	Shear Stiffness		(N)	1.00E+08				
	Torsion Stiffness		(N)	1.00E+08				
	Axial Stiffness	Rel. elongation	(mm/m)	3	1	0	-1	-3
		Axial force	(N)	1E+10	1E+08	0	-1E+08	-1E+10
Hydrodynamic Force	Quadratic Drag Coeff.		(-)	1.0				
	Added Mass Coeff.		(-)	1.0				

4.5. Time-domain setup

To evaluate the feasibility of the concept, a coupled time-domain method has been applied to perform sensitivity studies of the fish farm for different numbers of cages, wave conditions, and current velocities. The cases used in the time-domain simulations are described in this section. This study is limited to analyzing the effects on symmetrical models with two, four and six cage modules. Figure 20 shows the different cage and base module configurations for the models used in the coupled time-domain simulations.

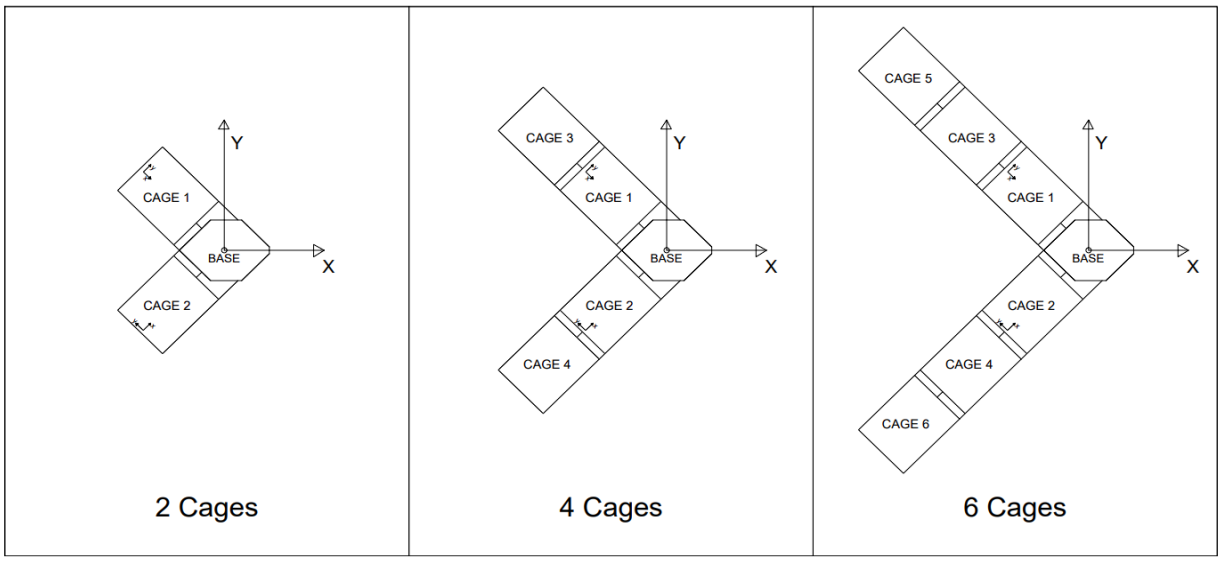

Figure 20. Different configurations of the cage and base modules.

Generally, environmental loads caused by natural phenomena such as wind, waves, and current are applied in complete studies, however, this study excludes wind loads due to the cage modules being mostly submerged, and at the current stage of the concept study, the preliminary design of the topside and superstructure of the base module has not been completed. This study uses irregular waves which were modeled by the JONSWAP spectra using significant wave height (*Hs*), spectral peak period (*Tp*), and 3.3 peak enhancement factor parameters. Table 5 describes the different wave conditions used in the time-domain simulations. Tailored time histories, and the spectral power densities of the three generated wave conditions used in this study can be seen in Appendix A: Wave conditions.

Table 5. Wave conditions

WC no.	*Hs (m)*	*Tp (s)*
WC1	1.5	7
WC2	3	9
WC3	5	11

The environmental conditions should be representative of where the structure will be situated (DNV, 2014), therefore, this study uses similar environmental conditions presented in the numerical modeling validation and model testing study of "Ocean-Farm 1" (Jin et al., 2021), where the 100-year condition consists of *Hs* = 5 m, *Tp* = 11 s, current velocity = 0.75 m/s, and wind

velocity = 30 m/s. Table 6 shows the simulation matrix for the cases that have been studied in this paper.

Table 6. Time-domain simulation matrix

No. Of Cages	Wave Condition	Uc (m/s)	Dir_w[1]/Dir_c[2] (deg)
2	WC1 WC2 WC3	0.25	180
4	WC1 WC2 WC3	0.25	180
6	WC1 WC2 WC3	0.25	180
6	WC3	0.25 0.50 0.75	180

[1] Wave direction
[2] Current direction

A collection of 11 different cases has been used to study the global responses of the fish farm in different conditions. As shown in Table 6, sensitivity studies are performed on three models with different numbers of cages in three different wave conditions with the same current velocity, and the six-cage model in one wave condition with three different current velocities. To evaluate the effect of the number of cages and the different wave conditions on the global responses, the same current velocity was applied in simulations for the three models in the three wave conditions. To evaluate the effect of the current velocity, time-domain simulations were performed with three different current velocities for the six-cage model in the same wave condition.

The time-domain simulations have been performed for 3-hour simulation lengths, with a time step of 0.05 seconds. Time-histories for the motion results have been stored for each time step, and the results for the forces in the mooring lines and connectors have been stored every 4th time step. Subsequently, the initial transient phase of the time-histories has been discarded for analyzing the data.

Chapter Five

RESULTS & DISCUSSION

5.1. Global motion responses

Given the weather-vanning capabilities of the fish farm, the symmetry about the x-axis, and the alignment of the directions of the waves and current, this study focuses on the three most critical motions: surge, heave and pitch. This section presents results from the time-domain simulations where the effects on the motions due to different wave conditions, numbers of cages, and current velocity are discussed.

The time-histories for the surge motion (displacement in x-direction), heave motion (displacement in z-direction), and the pitch motion (y-rotation about C.O.G.) of the base module in different wave conditions, different module configurations, and current velocities are demonstrated in Figure 21, Figure 22, and Figure 26, respectively. Figure 21 compares the effects different wave conditions may have on the one model with the same current velocity.

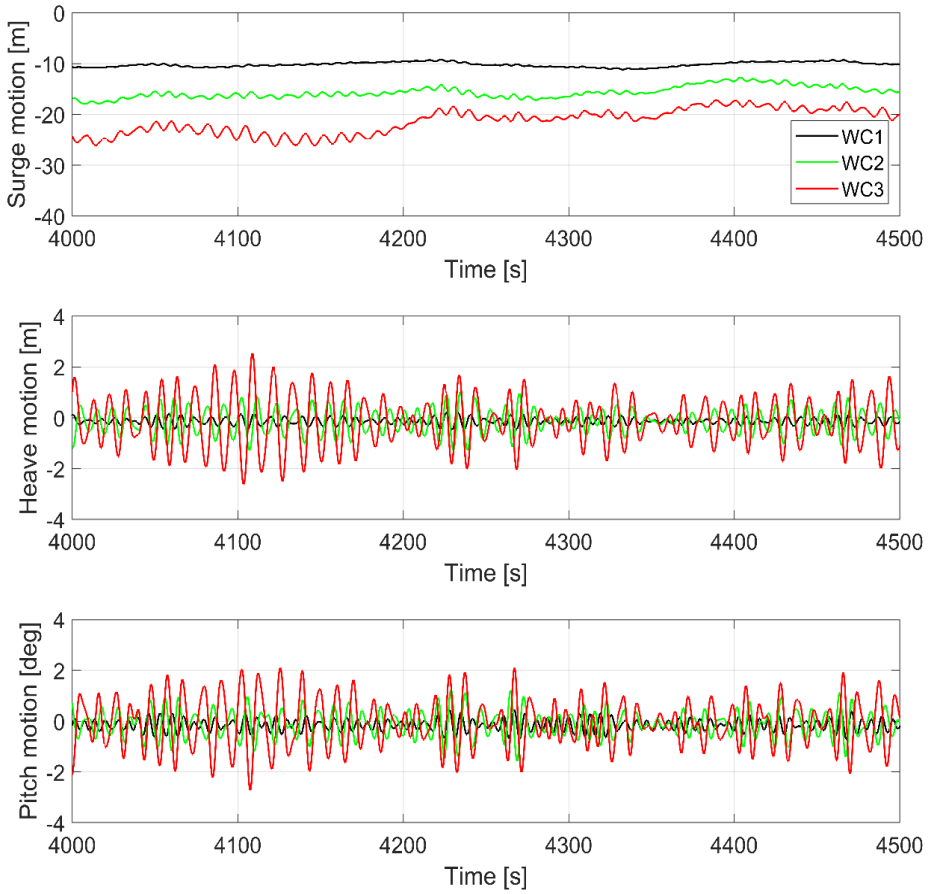

Figure 21. Selected response time histories of the base for the model with 6 cages for three environmental conditions: WC1, WC2, and WC3. All conditions with current velocity of 0.25 m/s.

Figure 21 illustrates that the surge motion oscillates with both wave frequency (WF) and low frequency (LF) components, whereas the heave and the pitch motions oscillate mainly with wave frequency components. It can be observed that the most extreme wave condition (WC3) causes the largest oscillation magnitudes in the WF components of the motions due to the larger linear wave forces acting on the system. The increase in low frequency mean drift forces in the more extreme wave conditions causes an increase in the LF component of the surge motion. The comparisons for the two and four cage models in different wave conditions are shown in Appendix B: Global motion responses.

Figure 22 shows the time-histories for models with two, four, and six cages in WC3 and a current velocity of 0.25 m/s. It provides insights into a design standard related to the capacity of the aquaculture system.

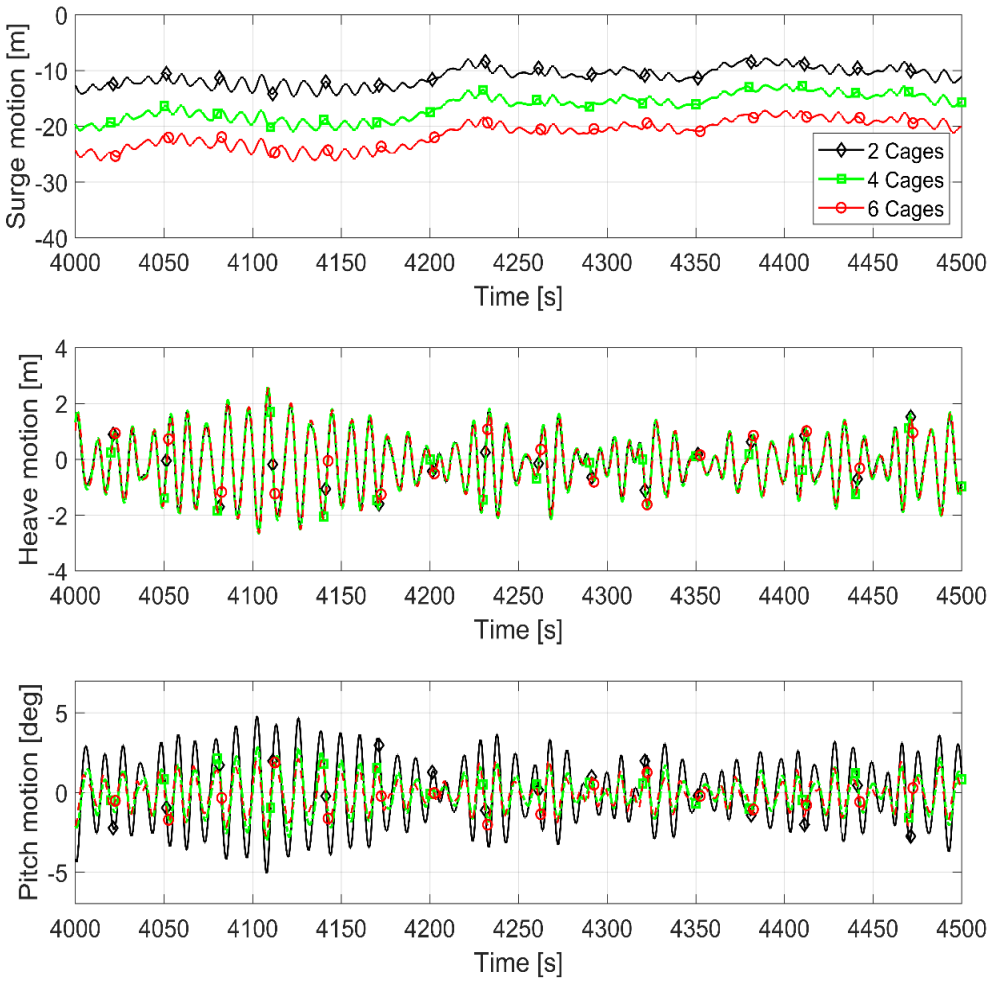

Figure 22. Selected response time histories the base module for models with 2, 4 and 6 cages in WC3 and current velocity of 0.25 m/s.

It can be observed in Figure 22 that the number of cages has minor effect on the heave motion. This is attributed to the relatively small waterplane area of the cages compared to the base module. Additionally, the number of cages principally affects the mean surge and not the pitch oscillation. As the number of cages increases, there are more elements in the system that are subjected to drag forces from the current and mean wave drift forces. The increased drag force causes the mean displacement in the negative x-direction to increase. The comparisons for the numbers of cages in WC1 and WC2 are shown in Appendix B: Global motion responses.

Larger surge displacement suggests that there is a larger force acting on the base-module at the point of connection to the cage-modules in the negative x-direction, which also causes the restoring

force from the mooring lines on the base-module in the positive x-direction to increase. These forces acting in opposite directions create a constraint on the pitch motion of the base-module.

Figure 23 presents the standard deviations of the heave and pitch motions for the 2, 4 and 6-cage models in the three environmental conditions WC1, WC2, and WC3 with the same current velocity of 0.25 m/s.

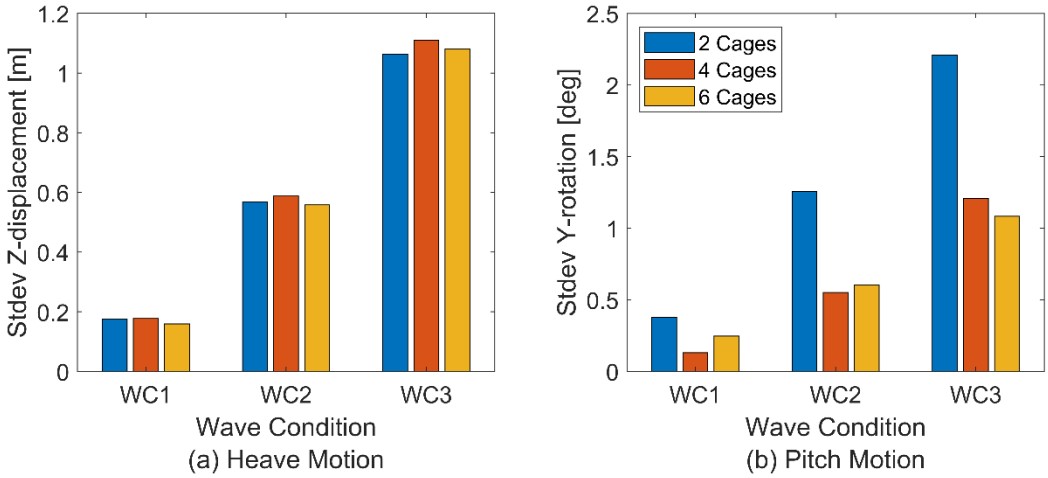

Figure 23. Standard deviations of heave (a) and pitch (b) motions for cage numbers and different wave conditions with current velocity of 0.25 m/s.

Generally, the standard deviation of the heave and pitch motions for all models increases as the wave condition becomes more extreme. The standard deviations of the heave motion for the models with different number of cages reflect that heave responses are not affected by the hydrodynamic loads on the cages, as can be seen in Figure 23(a). The standard deviation of the pitch motion for the 2-cage model is significantly higher than the other models in the three environmental conditions, whereas the 4 and 6-cage models show similar standard deviations.

The spectral power densities for the surge motions of the three models in the three wave conditions with current velocities of 0.25 m/s are presented in Figure 24.

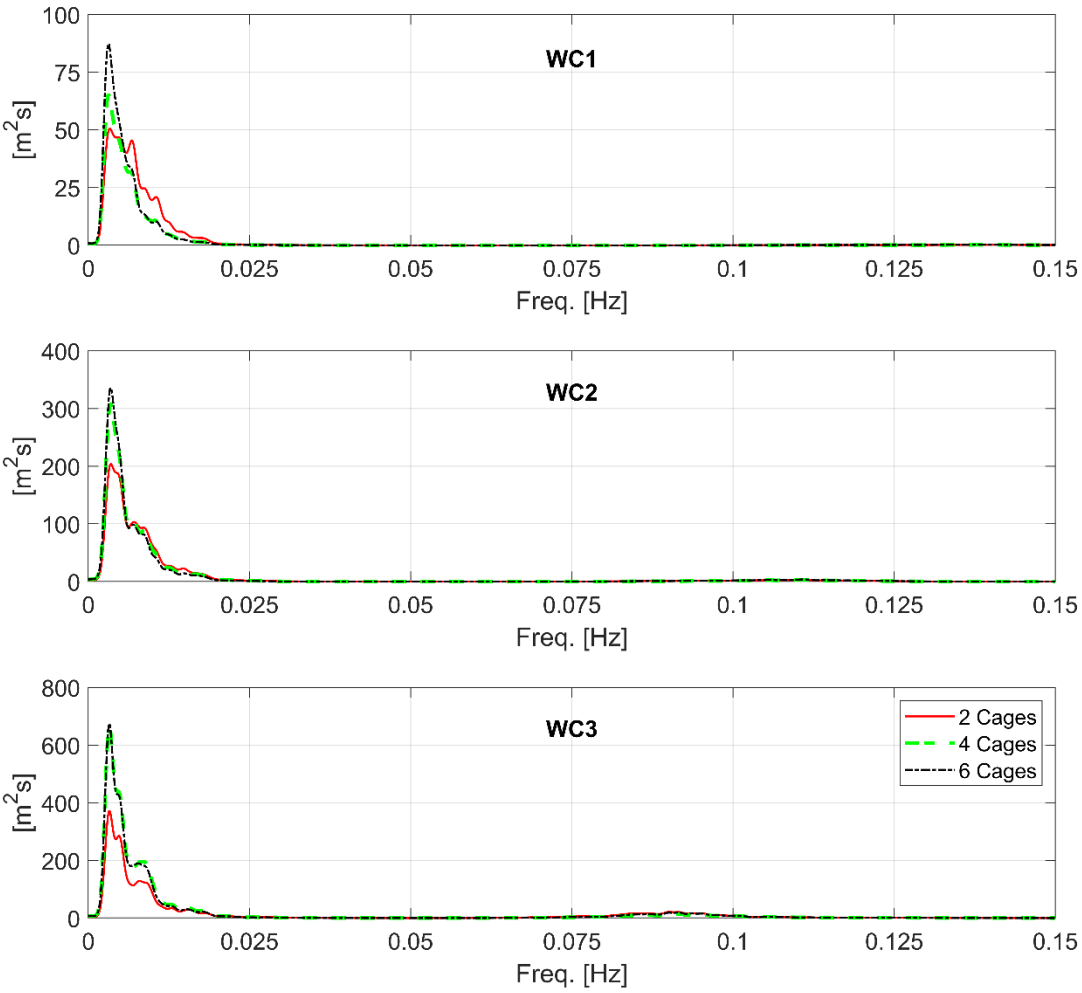

Figure 24. Surge motion power density spectrum of the 2, 4 and 6-cage models in different wave conditions with 0.25 m/s current velocity.

In all cases, the surge motions are dominated by the LF components, which in this study are considered frequencies below 0.05 Hz (period above 20 s), and display peaks around frequencies corresponding to 100, 150, 200, and 300-second periods. For WC1, the 2-cage model displays the largest magnitude at 100 and 150 s periods, and lowest magnitudes at 200 and 300-second periods. For WC2, the three models display similar magnitudes at 100 and 150-second periods. For lower frequencies, the 2-cage model has a lower magnitude, while the responses of the 4 and 6-cage models are similar. For WC3, the surge responses of the 4 and 6-cage models have similar spectral densities, and that of the 2-cage module has lower magnitudes in the LF range.

To better understand the effects of the number of cages and the wave conditions on the surge motion, the mean value for the x-displacement and the standard deviations of the LF and WF components of the dynamic surge motions are presented in Figure 11.

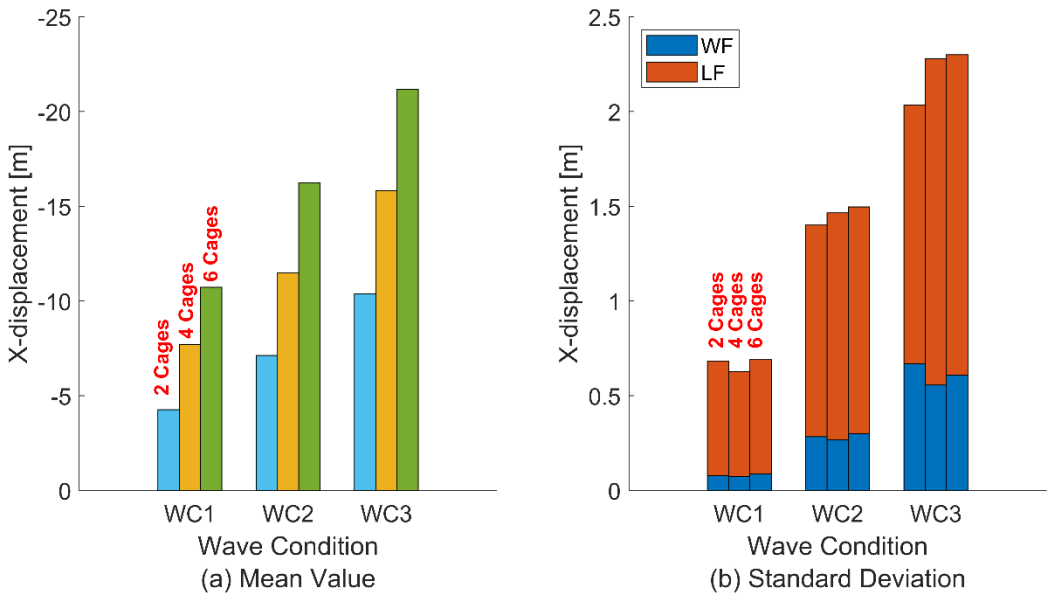

Figure 25. Mean values for the x-displacement (a) and standard deviations of the wave and low frequency components of the surge motion (b) for the 2, 4 and 6-cage model in WC1, WC2 and WC3 with a current velocity of 0.25 m/s.

As previously discussed, the mean x-displacement increases as the number of cages increases and as the environmental conditions become more extreme, which can also be seen in Figure 25(a). Additionally, the dynamic movements in the x-direction increase with more extreme wave conditions, but the results presented in Figure 25(b) imply that there isn't a conclusive relationship between the number of cages and the dynamic movements in the x-direction. The WF and LF standard deviations also demonstrate that LF components dominate the surge motions and increase with more extreme wave conditions, which was evident in the power density spectrums previously presented in Figure 24.

The previous results demonstrate the influence on the motions of the base-module from different amounts of cage-modules and wave conditions. To study the effects of current velocities on the motions of the base-module, the surge, heave, and pitch responses of the 6-cage model in WC3

with different current velocities are compared. The tailored time series (4000-4500s) in the 3 DOFs are displayed in Figure 26.

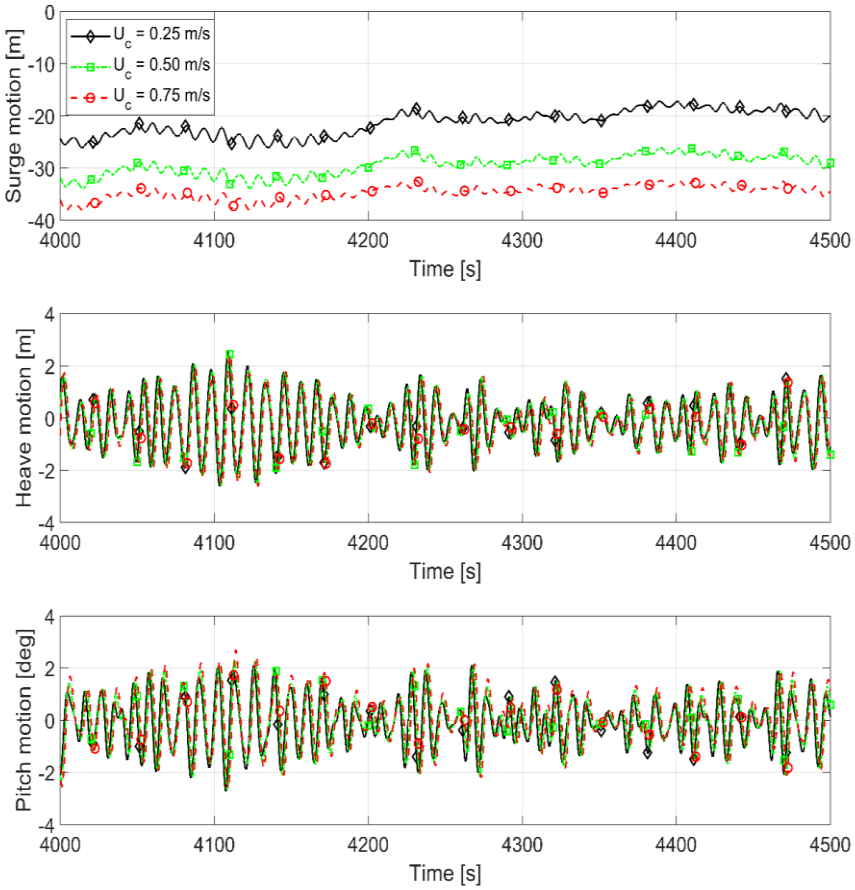

Figure 26. Selected time histories of motions for the 6-cage model in WC3 with different current velocities.

It can be noticed from Figure 26 that an increase in current velocity leads to an increased mean surge of the base module, which can be attributed to increased drag forces on the system. Additionally, the effect of the current velocity on the heave and pitch motions is minimal.

To better understand the effect of the current velocity on the surge motion, the mean values, and standard deviations of the LF and WF components are presented in Figure 27.

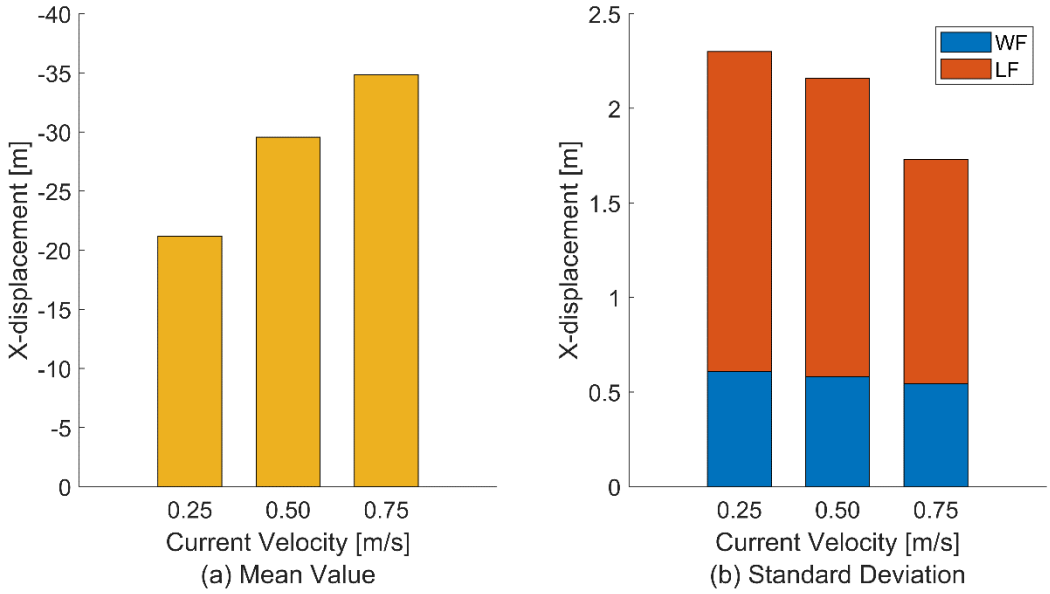

Figure 27. Mean values for the x-displacement (a) and standard deviations of the wave and low frequency components of the surge motion (b) for the 6-cage model in WC3 and different current velocities.

As expected, Figure 27(a) shows that the mean surge displacements increase with higher current velocities since drag force is a function of fluid velocity. Figure 27(b) suggests increasing the current velocity reduces the low-frequency dynamic surge motions.

5.2. Mooring line tension

The following section focuses on the results of tension in the mooring lines from the time-domain simulation. The tensions correspond to the segment of the mooring line where it is connected to the turret on the base module. Due to the symmetry and weather-vanning capabilities of the fish-farm, and the direction of the waves and current, only the results for mooring lines 1 through 4 are presented. To compare the tension in mooring lines 1 through 4, Figure 28 shows the time-histories of the 6-cage model in WC3 and a current velocity of 0.25 m/s.

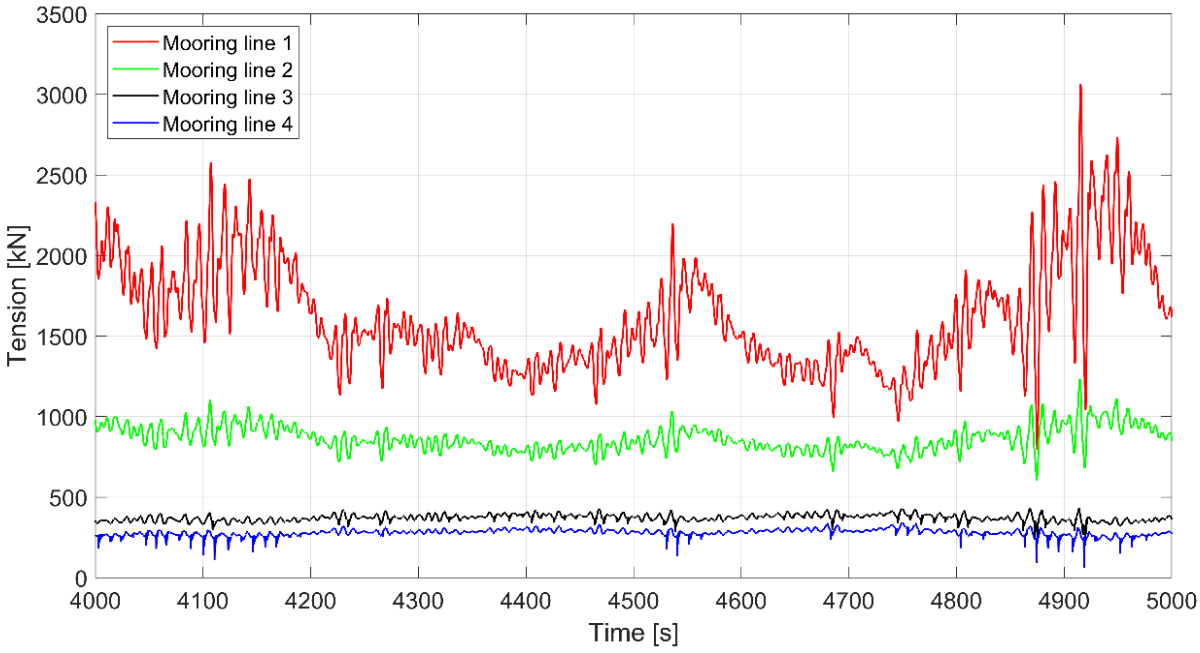

Figure 28.Selected time-histories of the tension in different mooring lines for the 6-cage model in WC3 with a current velocity of 0.25 m/s.

As can be observed in Figure 28, the tension in the mooring lines oscillate with both WF and LF components. Additionally, as would be assumed by the set-up of the mooring lines, and the wave and current directions, mooring line 1 experiences the largest mean tension followed by mooring lines 2, 3 and 4. It is also shown that the amplitudes in the oscillations in the WF and LF components of the tension are the largest for mooring line 1. Tailored time histories for the tension in mooring line 1 for all cases with current velocity of 0.25 m/s are presented in Appendix C: Mooring line tension.

To compare the effect of the number of cages in the fish farm, and the wave conditions, the 3-hour maximum tension in mooring lines 1-4 for different models and wave conditions with the same current velocity are presented in Figure 29.

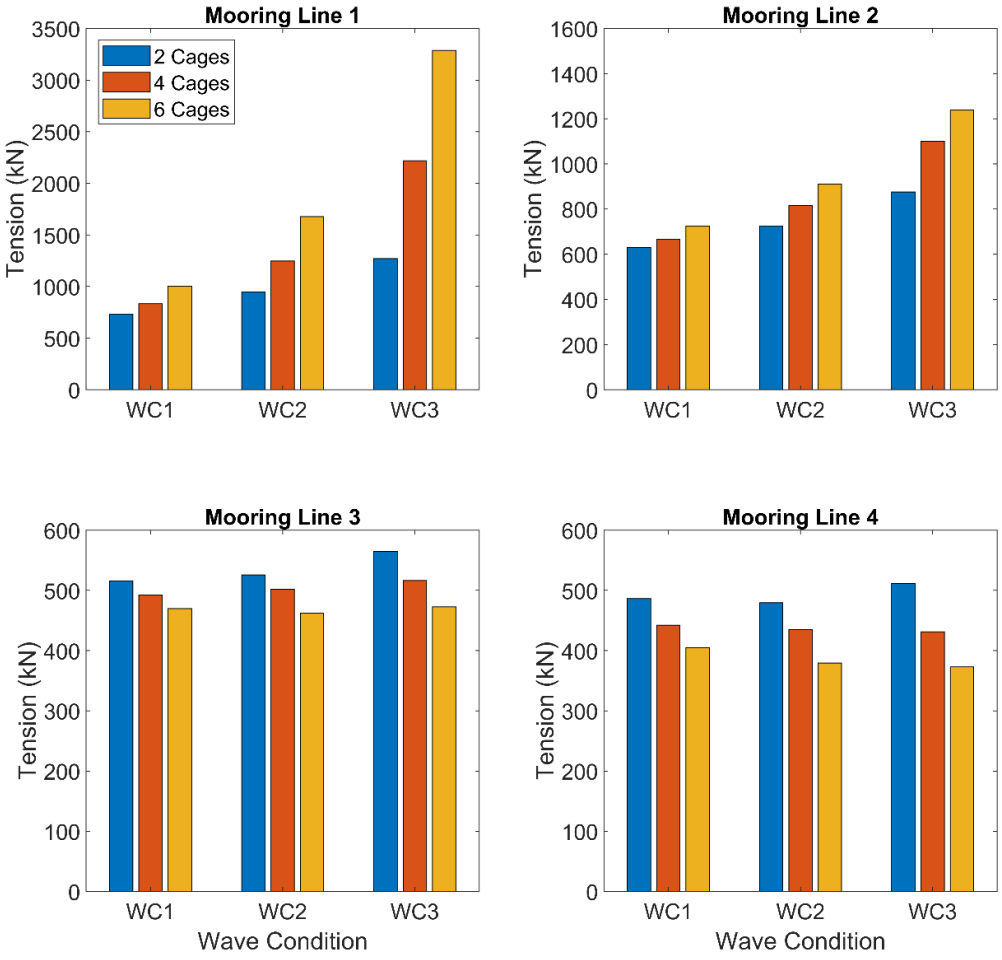

Figure 29. Comparison of 3-hr maximum tension for mooring lines 1-4 of different models in different wave conditions with a current velocity of 0.25 m/s.

As can be observed in Figure 29, the 3-hour maximum tension in mooring lines 1 and 2 increase with an increasing number of cages and with more extreme wave conditions. The 3-hour maximum tension in mooring lines 3 and 4 decreases with additional cages and does not show much variation due to different wave conditions.

It is clear from the results shown in Figure 28 and Figure 29, that mooring line 1 is the most critical in this set-up, therefore, the remainder of this chapter focuses on comparing results for mooring line 1 in different models, conditions, and current velocities. The power density spectrum of mooring line 1 comparing the effects of the wave condition, the number of cages, and the current velocity are presented in Figure 30.

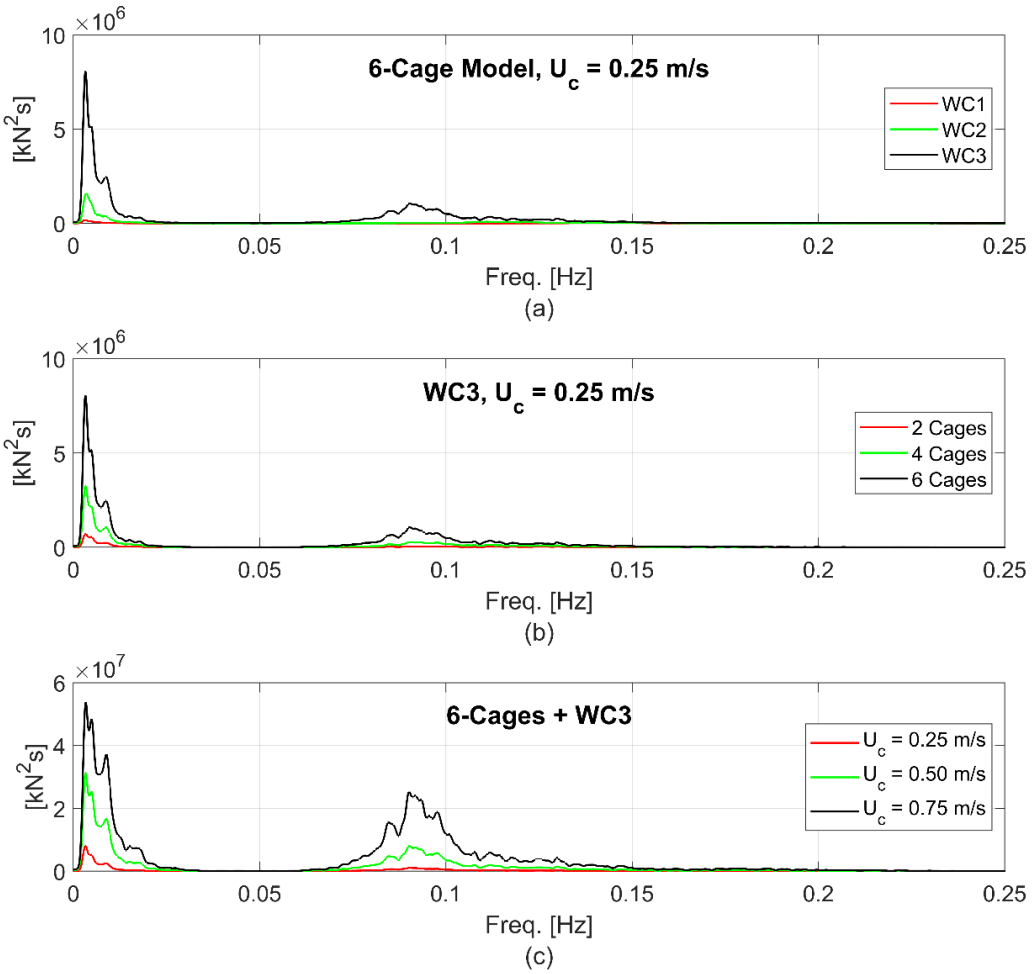

Figure 30. Mooring line 1 tension spectrums comparing the effect of the wave condition for the 6-cage model (a) and comparing different models in WC3, where both (a) and (b) have a current velocity of 0.25 m/s. Figure (c) compares the effect of current velocities

Figure 30 confirms the previous findings discussed for Figure 28, in which the presence of both LF and WF components in the oscillations of the tension in the mooring lines are observed. Additionally, it shows that more extreme wave conditions, more cages, and a higher current velocity increase the magnitude of the power density in both the LF and WF components. Similar to the surge motions, the LF component of the tension has peaks near frequencies corresponding to 100, 200, and 300 second periods. Additional spectrums for all cases with 0.25 m/s current velocity are presented in Appendix C: Mooring line tension.

The comparison of the mean tension in mooring line 1 and the standard deviations of the WF and LF components for all models and wave conditions with the same current velocity are presented in Figure 31(a), and for the 6-cage model in WC3 with different current velocities in Figure 31(b).

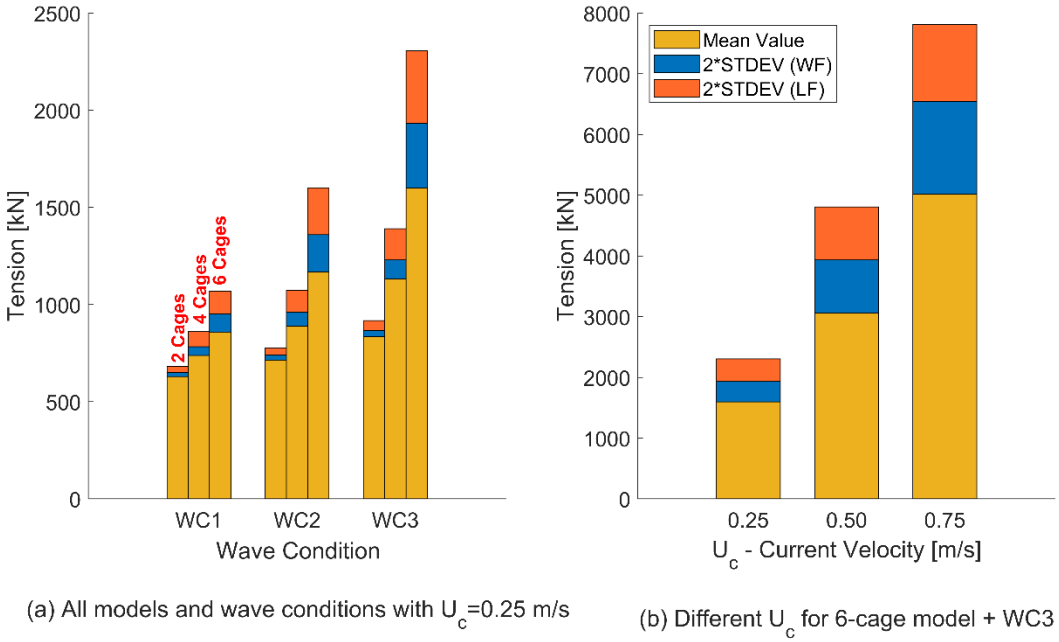

(a) All models and wave conditions with U_c=0.25 m/s

(b) Different U_c for 6-cage model + WC3

Figure 31. Comparison of mean, WF and LF component standard deviations of the tension in mooring line 1 for (a) all models and all wave conditions with the same current, and for (b) 6-cage model in WC3 with different current velocities (b)

As can be observed in Figure 31, the mean tension in mooring line 1 becomes larger in more extreme wave conditions, and as the number of cages and the current velocity increase. The mean tension in mooring line 1 is correlated to the catenary shape of the mooring line, which is affected by the displacement of the base-module in the x-direction. This horizontal displacement causes more of the mooring line to be elevated off the seabed, effectively increasing the tension in the line.

Figure 31 also shows larger standard deviations in the WF and LF components with more extreme wave conditions, a larger number of cages, and increased current velocity. The increase in the dynamic tensions of the mooring line for the more extreme cases is also attributed to the catenary shape of the mooring line. As the mean surge displacement increases, the angle between the segment of mooring line 1 nearest to the base-module and the x-axis decreases, causing an increase in the effect the dynamic surge and pitch motions have on the tension in the mooring line.

5.3. Axial force in the module connectors

To get a preliminary overview for the design of the connectors between the modules, the following section analyzes the axial forces exerted on the module connectors for models with different numbers of cages, different wave conditions, and different current velocities. The following results are limited to the connectors on one row of cages due to the symmetry of the fish farm.

The connectors are identified as interior (I_n), middle (M_n), and exterior (E_n), where *n* denotes which modules are being connected. When $n = 1$, it refers to the connectors between the base-module and the first cage-module in the row. When $n = 2$, it refers to the connectors between the first and second cage-modules. When $n = 3$, it refers to the connectors between the second and third cage-modules.

The time-histories for the axial forces in the interior, middle, and exterior connectors between the base-module and the first cage-module are presented in Figure 32 to visualize the oscillations of the axial forces and their magnitudes.

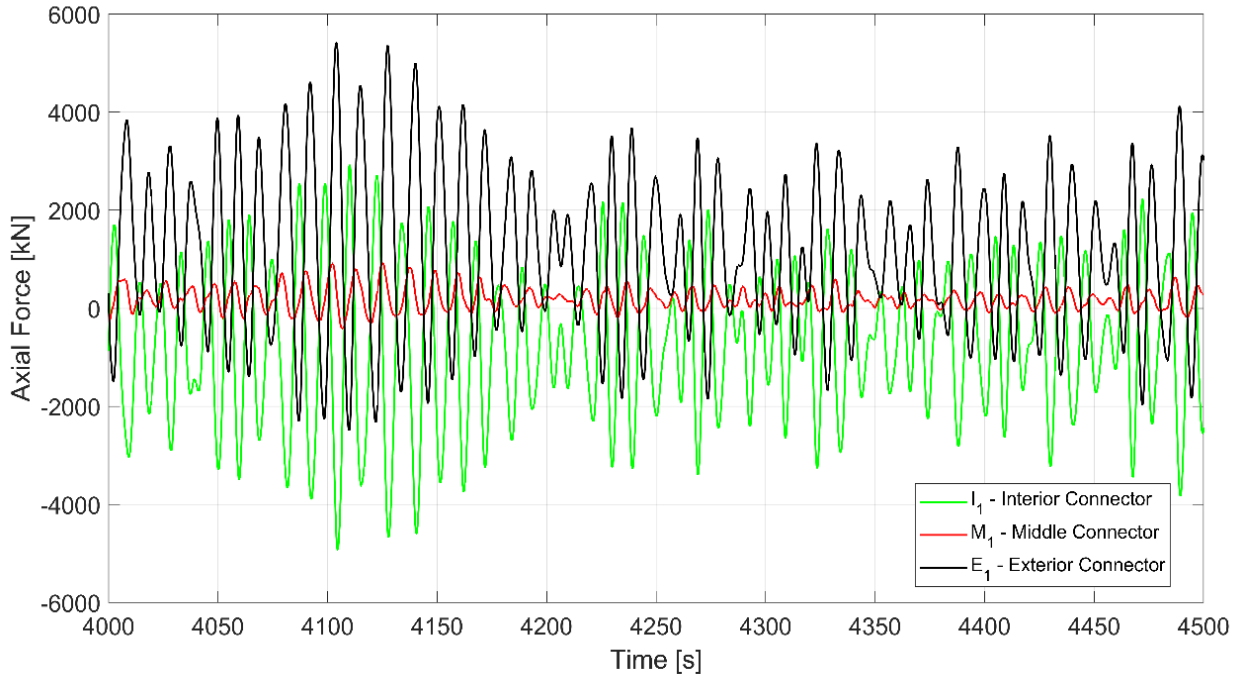

Figure 32. Selected time-histories for the axial force in connectors I_1, M_1, and E_1 for the 6-cage model in WC3 and a current velocity of 0.25 m/s.

The time-histories presented in Figure 32 exhibit that the axial forces in the connectors oscillate mainly with WF components. Additionally, it can be observed that the middle connector experiences much smaller oscillation amplitudes of axial force, and the interior and exterior connectors are opposite but have different mean values. To further evaluate the time-histories shown in Figure 32, the power density spectrum of the axial forces is presented in Figure 33.

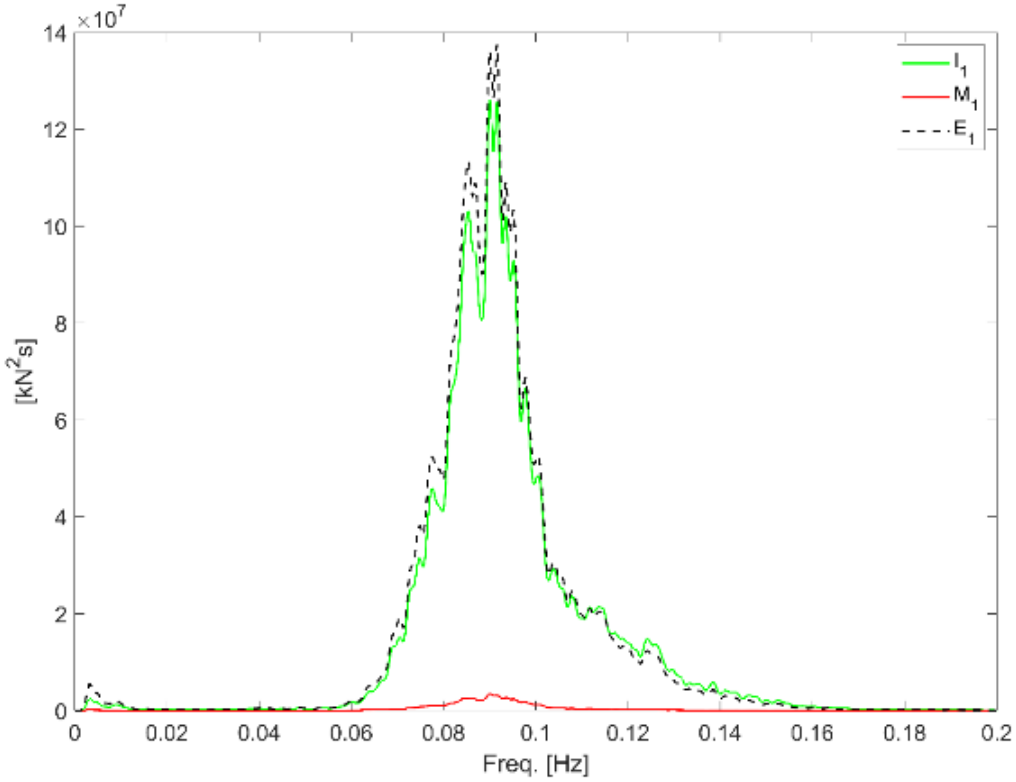

Figure 33. Axial force spectrum for the interior, middle, and exterior connectors between the base-module and the first cage-module for the 6-cage model in WC3 and a current velocity of 0.25 m/s.

The power density spectrum shown in Figure 33 confirms the previous observation about how the WF components dominate in the oscillations of the axial forces. Additionally, the similarity of the oscillations of axial forces for the interior and exterior connectors is also shown in the spectrum.

To compare the axial forces in connectors for different modules (n = 1:3) and locations (interior, middle, and exterior), Figure 34 shows the mean values and standard deviations for the 6-cage model in WC3 and a current velocity of 0.75 m/s.

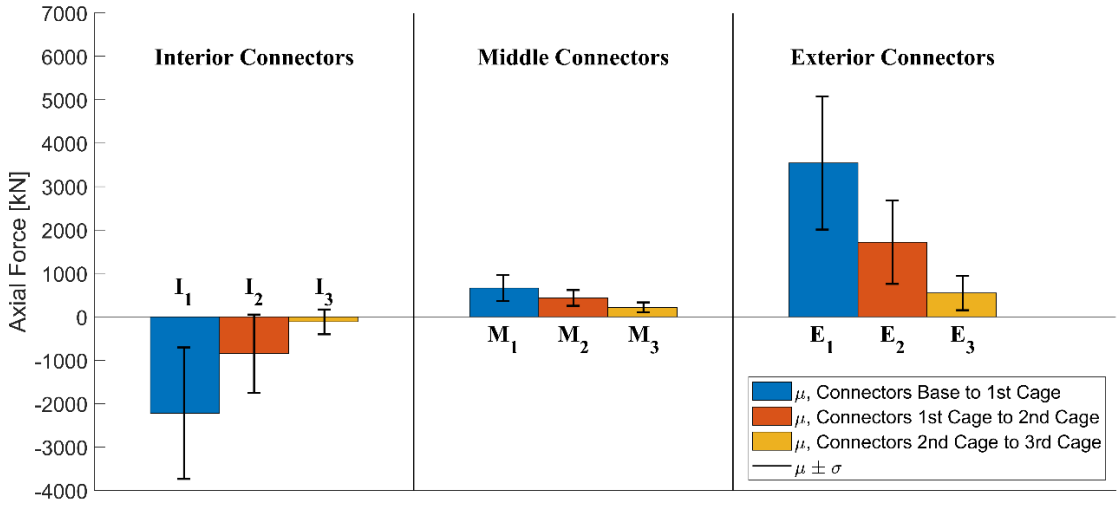

Figure 34. Comparison of the mean and standard deviation of the axial forces of all connectors for the 6-cage model in WC3 with a current velocity of 0.75 m/s.

As can be observed from Figure 34, the interior connectors have a negative mean axial force, whereas the middle and exterior connectors have a positive mean axial force. In this study, positive axial forces signify that the element is in tension, and negative axial forces signify that the element is in compression. It is also shown that the mean values and standard deviations are the largest for the exterior, middle and exterior connectors between the base-module and the first cage-module and decrease for the connectors between cage-modules the farther they are from the base.

Since the connectors between the base-module and the first experience the largest axial forces, the remainder of this section focuses on the effects on those connectors due to different numbers of cages in the model, different wave conditions and different current velocities.

Figure 35(a) compares the effect of having different numbers of cages, Figure 35(b) compares the effect of different wave conditions on the axial force, and Figure 35(c) compares the effect of different current velocities on the axial force of the interior, middle, and exterior connector between the base-module and the first cage-module.

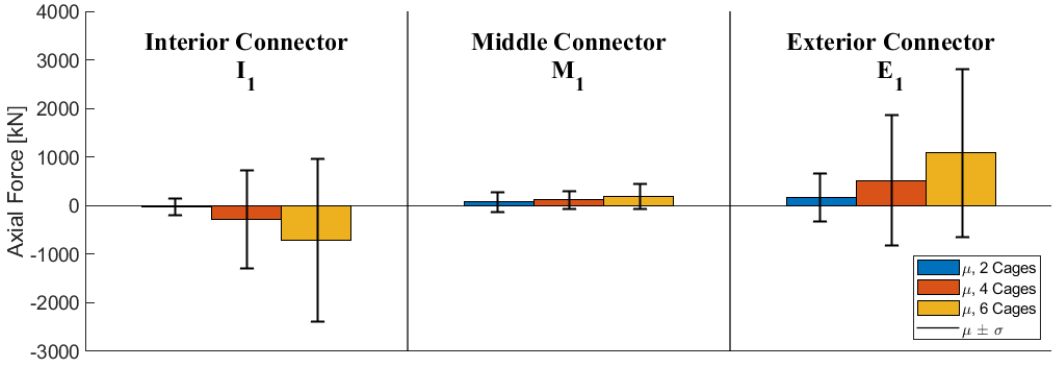

(a)

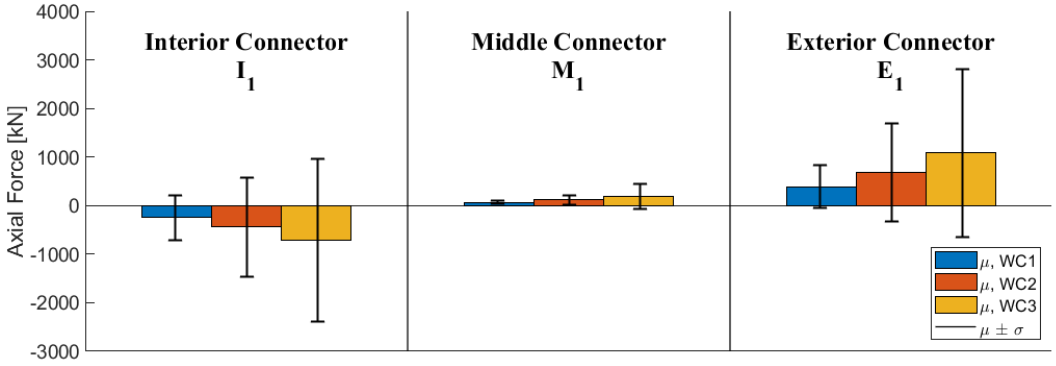

(b)

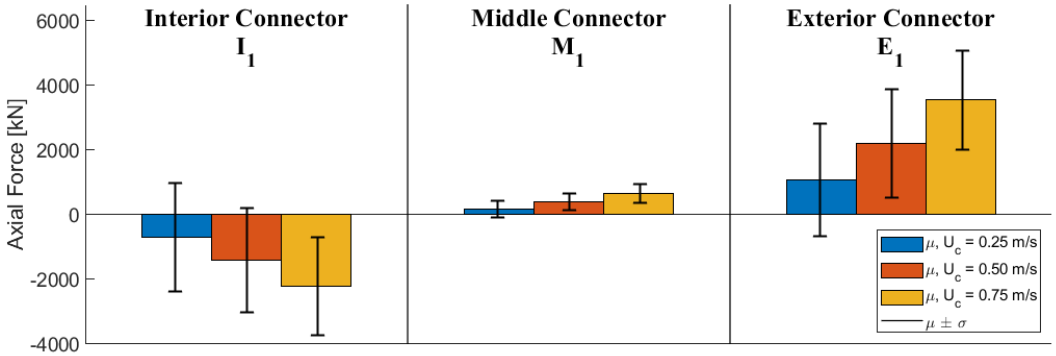

(c)

Figure 35. Comparison of the mean and standard deviations of the axial forces in the connectors between the base module and the 1st cage for (a) different numbers of cages in WC3 and a current velocity of 0.25 m/s. (b) the 6-cage model in different wave conditions and a current velocity of 0.25 m/s, and (c) the 6-cage model in WC3 with different current velocities.

As can be observed in Figure 35(a), for the three connectors between the base-module, there is an increase in mean axial force and the standard deviations of these forces. Additionally, the middle connector shows the least difference in these values for the three different models. The increase in

the mean axial forces for an increasing number of cages can be attributed to the increase in total drag force on the fish farm from the additional cage-modules causing larger reaction forces on the connectors. The increase in the standard deviations can be attributed to the increased inertia and damping from the larger number of cages, which requires more dynamic forces in the connectors to ensure the cages follow the motions of the base.

As can be observed in Figure 35(b), both the mean axial forces and the standard deviations increase with more extreme wave conditions. The increase in the mean axial forces can be attributed to the increasing drag forces in more extreme wave conditions. The increase in the standard deviations can be attributed to the increase in the motions of the base-module in more extreme wave conditions.

As can be observed in Figure 35(c), the mean axial forces increase as the current velocity increases, but the standard deviations are not affected. Increasing current velocities cause larger drag forces on the cage-modules, which increase the mean axial forces of the connectors. As was shown in Figure 26, the different current velocities have little effect on the dynamic motions of the base-module, which can also be seen in the similar standard deviations in the axial forces of the connectors. Comparisons of the mean and standard deviations of the axial force in the interior and exterior connector between the base-module and the first cage-module for all cases can be seen in Appendix D: Connector axial forces.

Chapter Six

CONCLUDING REMARKS & SUGGESTIONS FOR FUTURE WORK

6.1. Concluding remarks

This paper presents a study of a module-based offshore fish farm concept with a focus on the global motion responses, mooring analysis, and structural analysis of the module connectors. The focus is to compare the responses of such a system with different numbers of cage-modules, different wave conditions, and different current velocities. Corresponding numerical models of the concept have been established for the different modules, mooring and connectors. Subsequently, the coupled time-domain method has been applied for 3-hour long simulations. The main findings of this study are summarized as follows:

- Increasing the number of cages causes an increase in the mean surge displacement, a decrease in the pitch motion, and has little effect on the heave motion. Larger waves cause an increase in the three primary motions. Increasing the current velocity causes a larger mean surge displacement and does not have much effect on the heave and pitch motions.

- The mean and standard deviations of the tension in the critical mooring line are directly affected by additional cages, increasing the current velocity, and larger wave conditions.

- The axial forces in the connectors between the base-module and the first cage are the largest. The axial forces in the interior and exterior connectors experience similar oscillations which are dominated by the WF component. The addition of cages, higher current velocity, and larger waves increase the mean axial forces, while the dynamic axial forces are not sensitive to the current velocity.

6.2. Suggestions for future work

This study focuses on a preliminary feasibility study on the baseline design of the module-based offshore fish farm. Simplifications exist in the numerical model and numerical methods. The numerical model does not consider the effects of fluid velocity reduction caused by the wakes from the nets and the frame of the cage-modules. This simplification results in conservative results for both the global motions, the tension in mooring lines, and the axial forces in the connectors. The connectors are simplified as beam elements which may not represent the exact structural components. Regarding the environmental conditions, more simulation cases under different wave and current conditions, including misaligned waves and current directions, should be investigated. Moreover, sensitivity studies on solidity ratio of the nets and the configuration of the cages are also relevant. Future work should be devoted to addressing the above limitations.

REFERENCES

Aker Solutions. (2020, December 14). Aker Solutions Awarded First Fish Farm Assembly Contract. https://www.akersolutions.com/news/news-archive/2020/aker-solutions-awarded-first-fish-farm-assembly-contract/#

AKVA GROUP. (n.d.). Sea-based Marine Infrastructure. Retrieved December 6, 2022, from https://www.akvagroup.com/sea-based/marine-infrastructure/

Arctic Offshore Farming. (n.d.). Fact Sheet. Retrieved December 10, 2022, from https://www.arcticoffshorefarming.no/

Bi, C.-W., Zhao, Y.-P., Dong, G.-H., Xu, T.-J., & Gui, F.-K. (2013). Experimental investigation of the reduction in flow velocity downstream from a fishing net. Aquacultural Engineering, 57, 71–81. https://doi.org/10.1016/j.aquaeng.2013.08.002

Cheng, H., Li, L., Aarsæther, K. G., & Ong, M. C. (2020). Typical hydrodynamic models for aquaculture nets: A comparative study under pure current conditions. Aquacultural Engineering, 90. https://doi.org/10.1016/j.aquaeng.2020.102070

Cheng, H., Li, L., & Ong, M. C. (2022). Comparative study of five commonly used gravity type fish cages under pure current conditions. Ocean Engineering, 250, 110977. https://doi.org/10.1016/J.OCEANENG.2022.110977

DNV. (2008). Wadam theory manual. Det Norske Veritas.

DNV. (2014). Recommended Practice DNV-RP-C205, Environmental conditions and environmental loads. Det Norske Veritas.

DNV. (2021). Marine Aquaculture Forecast to 2050.

FAO. (2022). The State of World Fisheries and Aquaculture 2022. Towards Blue Transformation,. FAO. https://doi.org/10.4060/cc0461en

Gansel, L. C., Oppedal, F., Birkevold, J., & Tuene, S. A. (2018). Drag forces and deformation of aquaculture cages—Full-scale towing tests in the field. Aquacultural Engineering, 81, 46–56. https://doi.org/10.1016/J.AQUAENG.2018.02.001

Gomez-Uchida, D., Sepúlveda, M., Ernst, B., Contador, T. A., Neira, S., & Harrod, C. (2018). Chile's salmon escape demands action. Science, 361(6405), 857–858. https://doi.org/10.1126/science.aau7973

Google. (n.d.). Google maps.

Jin, J., Su, B., Dou, R., Luan, C., Li, L., Nygaard, I., Fonseca, N., & Gao, Z. (2021). Numerical modelling of hydrodynamic responses of Ocean Farm 1 in waves and current and validation against model test measurements. Marine Structures, 78. https://doi.org/10.1016/j.marstruc.2021.103017

Lee, C. H. (1995). WAMIT theory manual. Department of Ocean Engineering, Massachusetts Institute of Technology.

Li, L., Jiang, Z., Høiland, A. V., & Ong, M. C. (2018). Numerical analysis of a vessel- shaped offshore fish farm. Journal of Offshore Mechanics and Arctic Engineering, 140(4). https://doi.org/10.1115/1.4039131

Li, L., Jiang, Z., Wang, J., & Ong, M. C. (2019). Numerical Study on the Heading Misalignment and Current Velocity Reduction of a Vessel-Shaped Offshore Fish Farm. Journal of Offshore Mechanics and Arctic Engineering, 141(5). https://doi.org/10.1115/1.4042266

Løland, G. (1991). Current forces on and flow through fish farms.

MARINTEK. (2015). RIFLEX User Manual Version 4.6. MARINTEK.

Miao, Y. ji, Ding, J., Tian, C., Chen, X. jun, & Fan, Y. li. (2021). Experimental and numerical study of a semi-submersible offshore fish farm under waves. Ocean Engineering, 225. https://doi.org/10.1016/j.oceaneng.2021.108794

Mjåtveit, M. A., Cheng, H., Ong, M. C., & Lee, J. (2022). Comparative study of circular and square gravity-based fish cages with different dimensions under pure current conditions. Aquacultural Engineering, 96, 102223. https://doi.org/10.1016/J.AQUAENG.2021.102223

Mobron, E., Torgersen, T., Zhu, S., Riis, J., & Bye, M. (2022). Design of Havfarm 1. In S. H. and W. C. M. and de G. D. R. Piatek Łukasz and Lim (Ed.), WCFS2020 (pp. 99–111). Springer Singapore.

Oppedal, F., Vågseth, T., Dempster, T., Juell, J. E., & Johansson, D. (2011). Fluctuating sea-cage environments modify the effects of stocking densities on production and welfare parameters of Atlantic salmon (Salmo salar L.). Aquaculture, 315(3–4), 361–368. https://doi.org/10.1016/J.AQUACULTURE.2011.02.037

RINA. (2021). Oceangoing Aquaculture Vessel Gains RINA Approval. https://www.rina.org/en/media/press/2021/11/23/fish-farm-vessel

SalMar ASA. (n.d.). Gallery. Retrieved November 21, 2022, from https://www.salmar.no/en/gallery/

SalMar ASA. (2022). Annual report 2021.

Sun, S., Li, H., Muk, C. O., & Li, L. (2022). Design load and yielding strength analyses of the floating structure of a truss-type offshore cage. Harbin Gongcheng Daxue Xuebao/Journal of Harbin Engineering University, 43(3). https://doi.org/10.11990/jheu.202101049

Tang, H., Xu, L., & Hu, F. (2018). Hydrodynamic characteristics of knotted and knotless purse seine netting panels as determined in a flume tank. PLOS ONE, 13(2), e0192206. https://doi.org/10.1371/journal.pone.0192206

Time, J. (n.d.). Huge Feed Barge with Major Environmental Benefits. Akva Group. Retrieved November 23, 2022, from https://www.akvagroup.com/news/huge-feed-barge-with-major-environmental-benefits

Trauthwein, G. (2020, November 12). Aquaculture: Inside the De Maas' Offshore Fish Farm. MarineLink. https://www.marinelink.com/news/aquaculture-inside-de-maas-offshore-fish-483165

Appendix

List of Appendices

Appendix A: Wave conditions

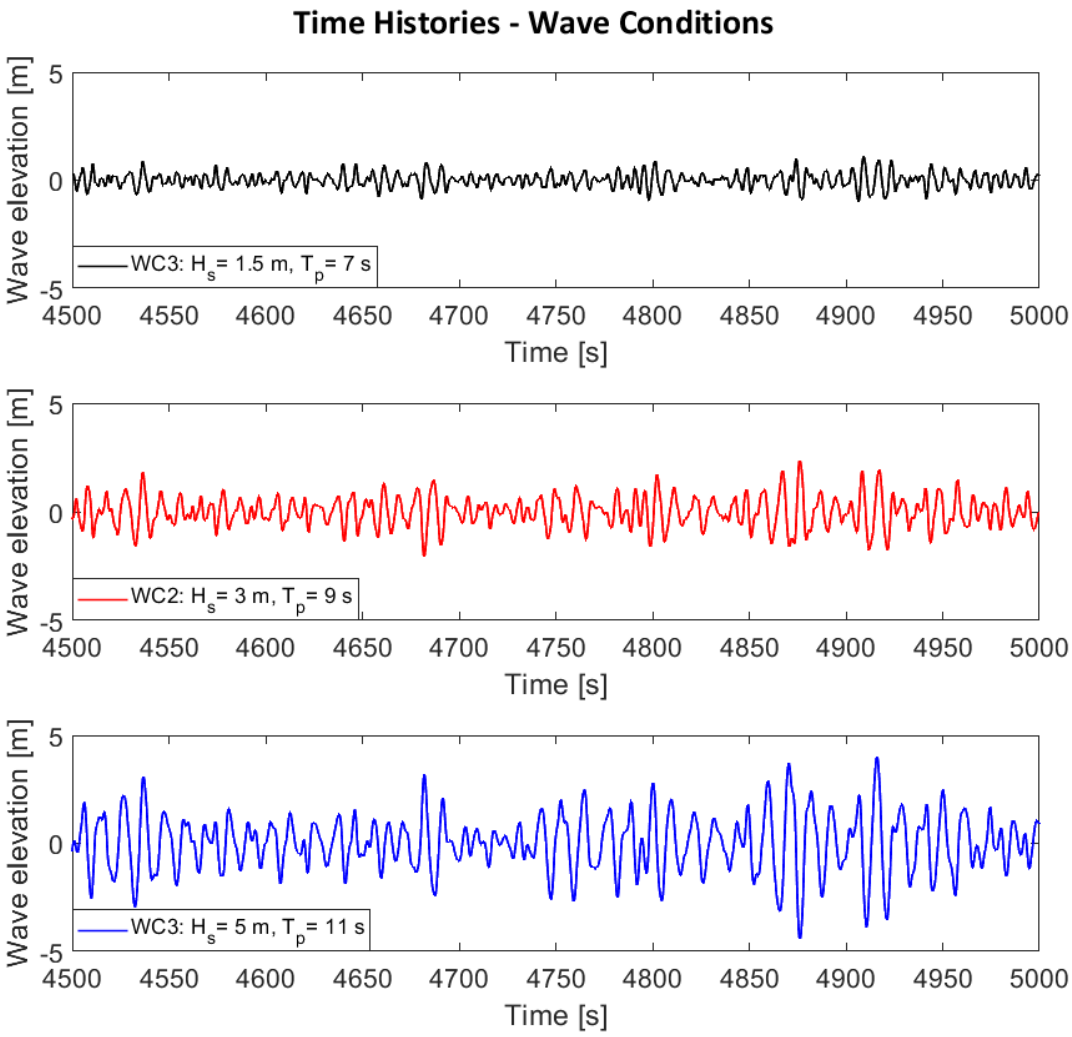

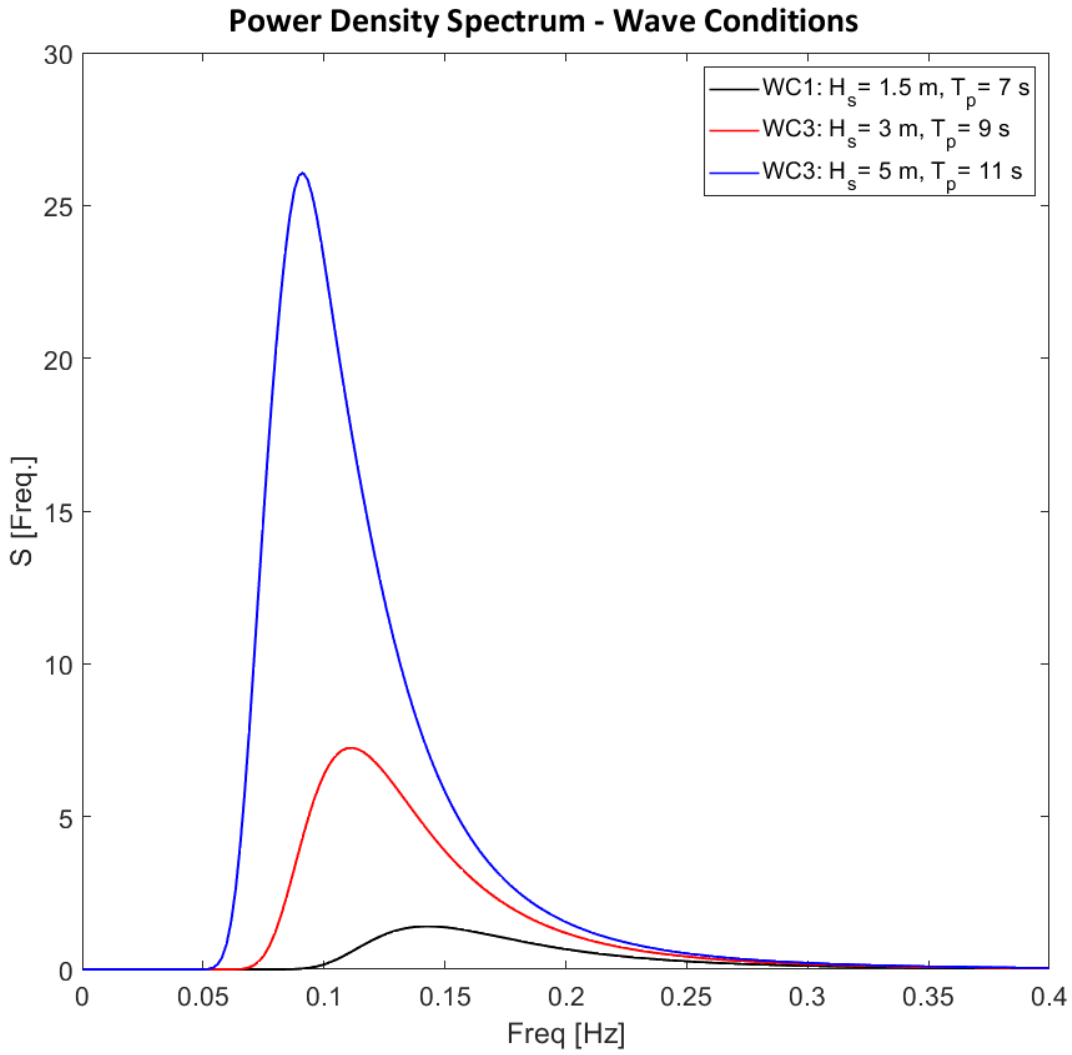
Power Density Spectrum - Wave Conditions
WC1: H_s = 1.5 m, T_p = 7 s
WC3: H_s = 3 m, T_p = 9 s
WC3: H_s = 5 m, T_p = 11 s
S [Freq.]
Freq [Hz]
0
5
10
15
20
25
30
0
0.05
0.1
0.15
0.2
0.25
0.3
0.35
0.4

Appendix B: Global motion responses

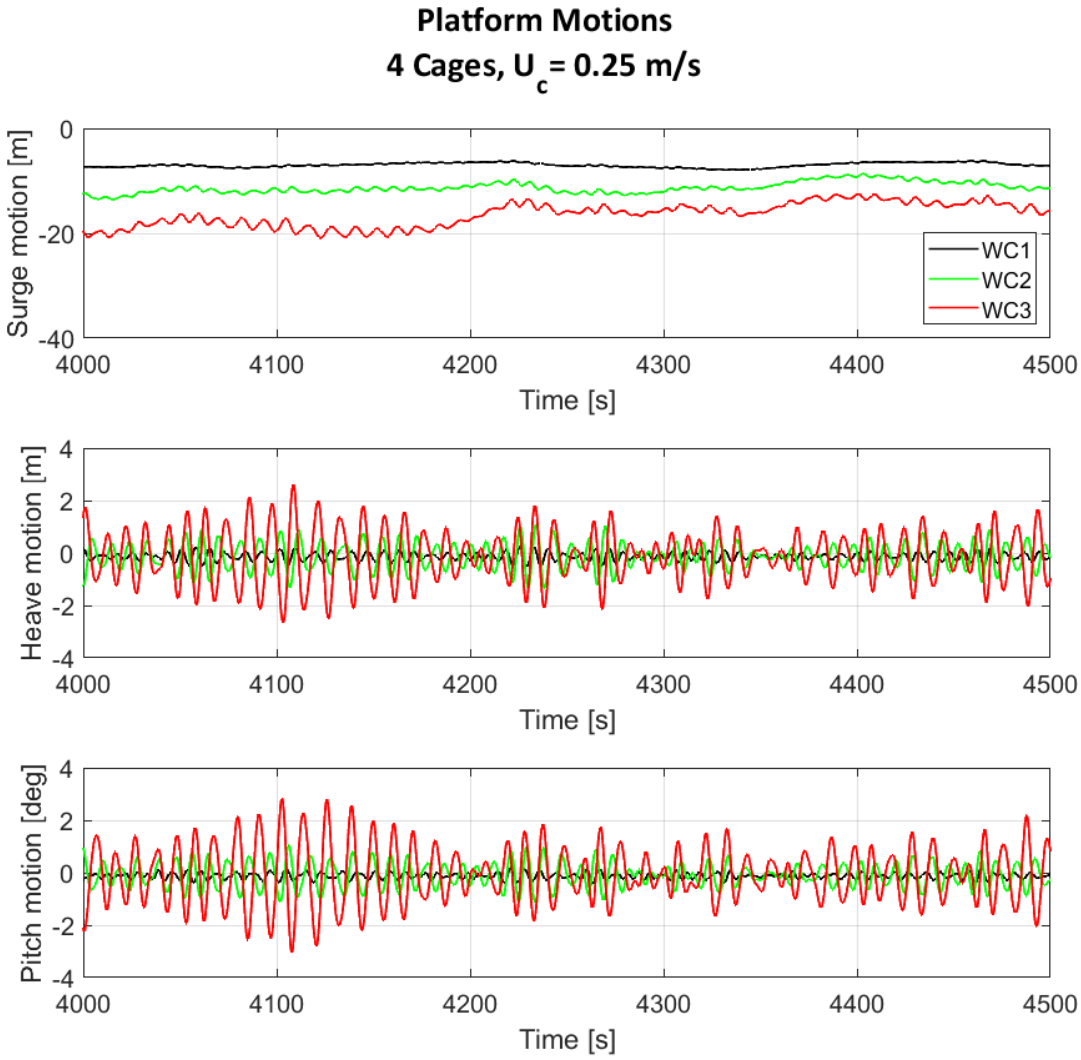

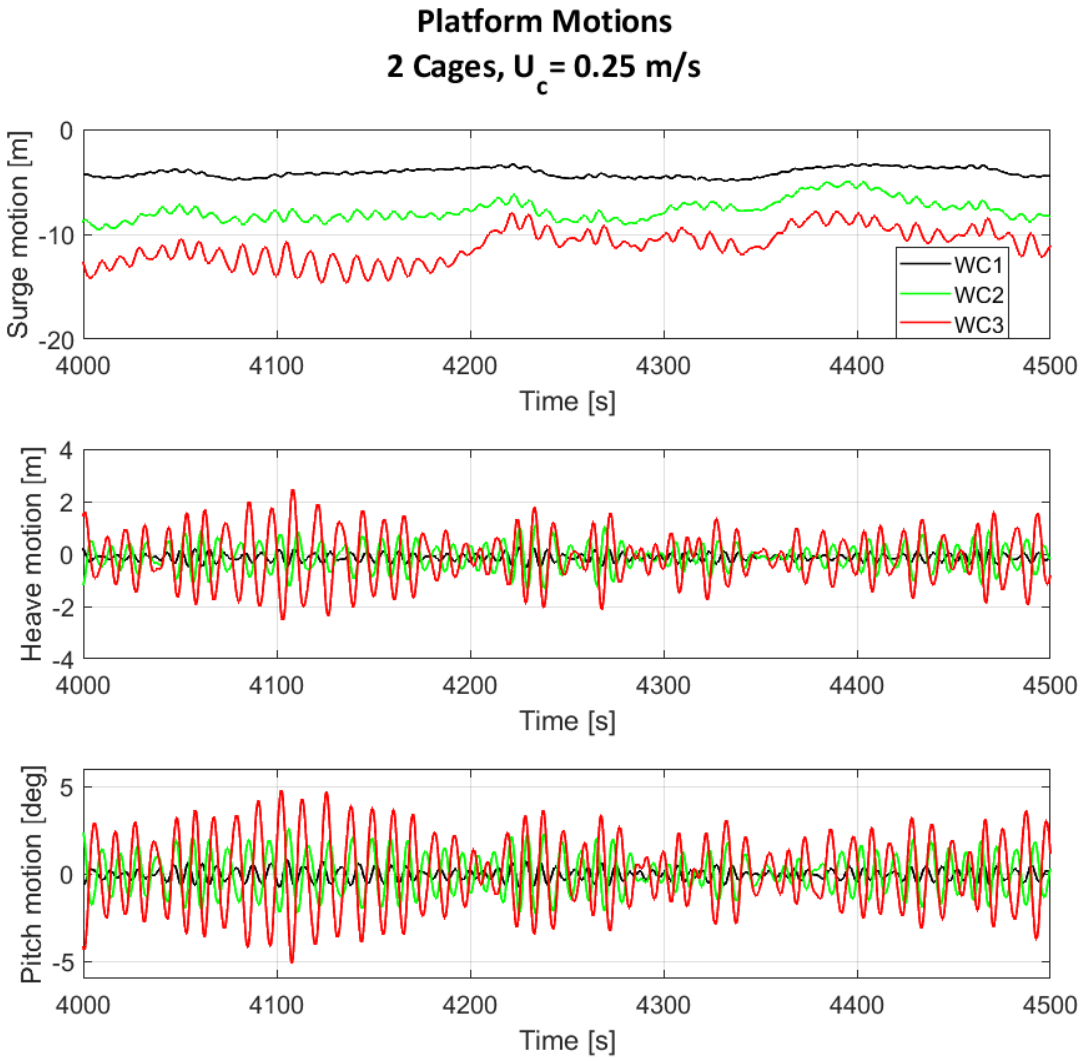
Platform Motions
2 Cages, U c = 0.25 m/s
Surge motion [m]
0
-10
-20
WC1
WC2
WC3
4000
4100
4200
4300
4400
4500
Time [s]
Heave motion [m]
4
2
0
-2
-4
Time [s]
Pitch motion [deg]
5
0
-5
Time [s]

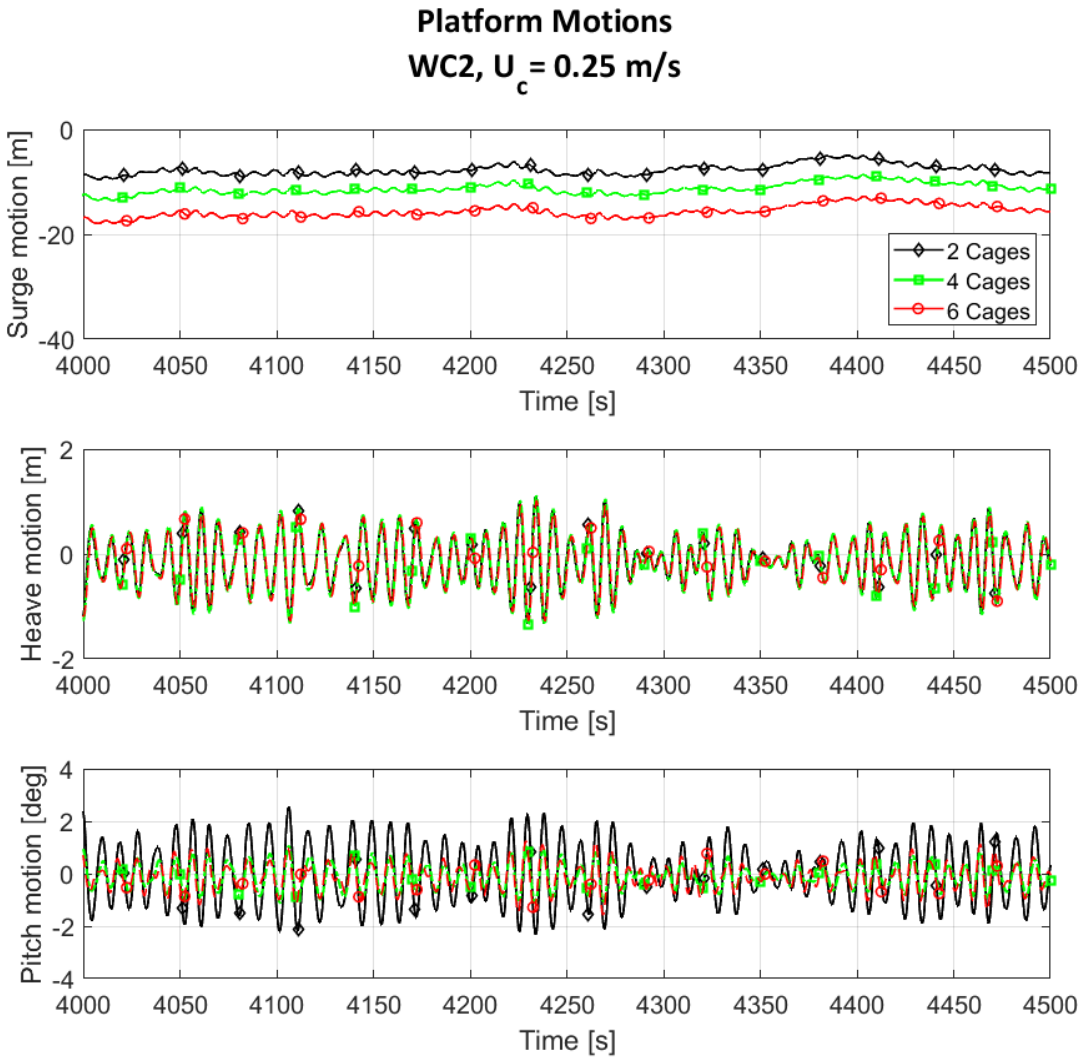
Platform Motions
WC2, U_c = 0.25 m/s
Surge motion [m]
Heave motion [m]
Pitch motion [deg]
Time [s]
2 Cages
4 Cages
6 Cages

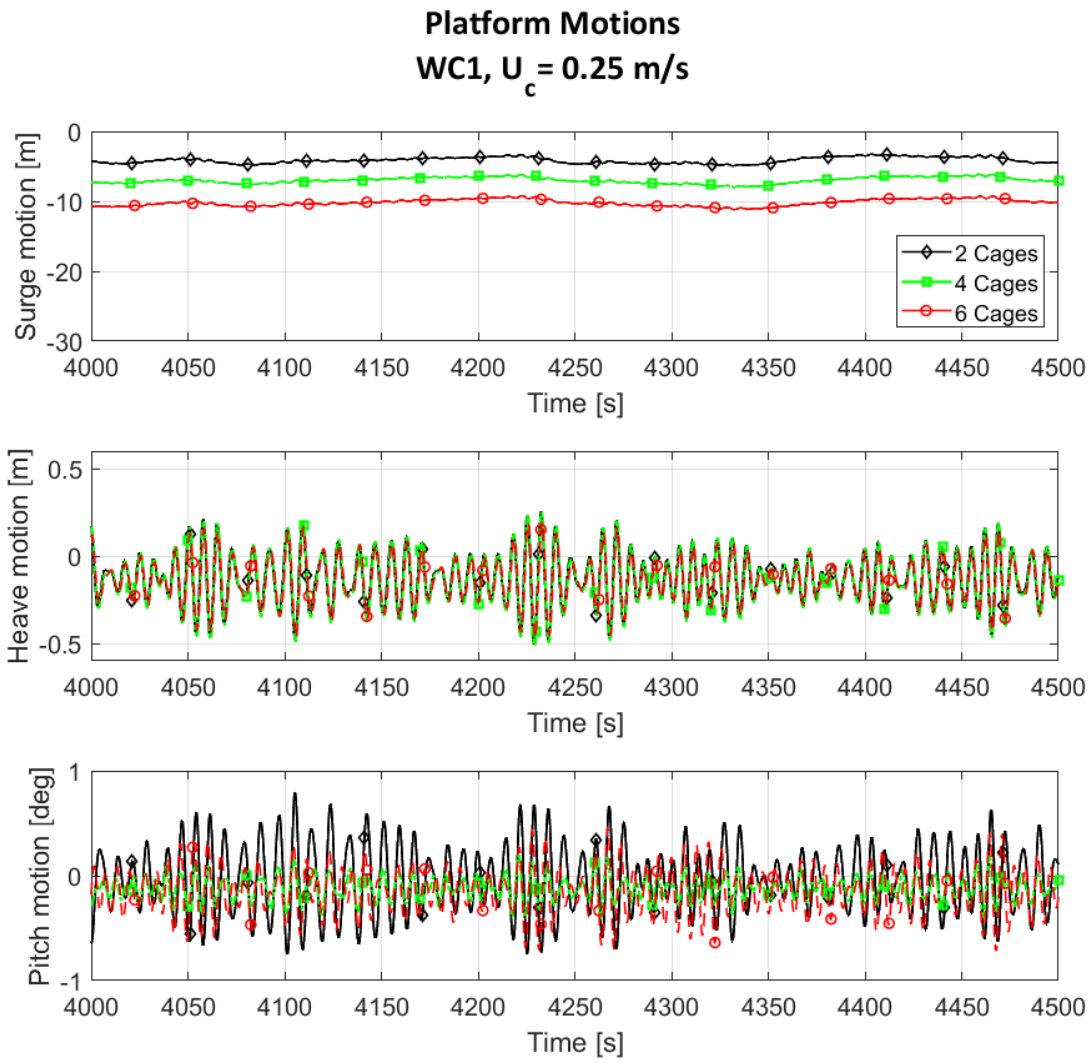
Platform Motions
WC1, U_c = 0.25 m/s
Surge motion [m]
Heave motion [m]
Pitch motion [deg]
Time [s]
2 Cages
4 Cages
6 Cages

Appendix C: Mooring line tension

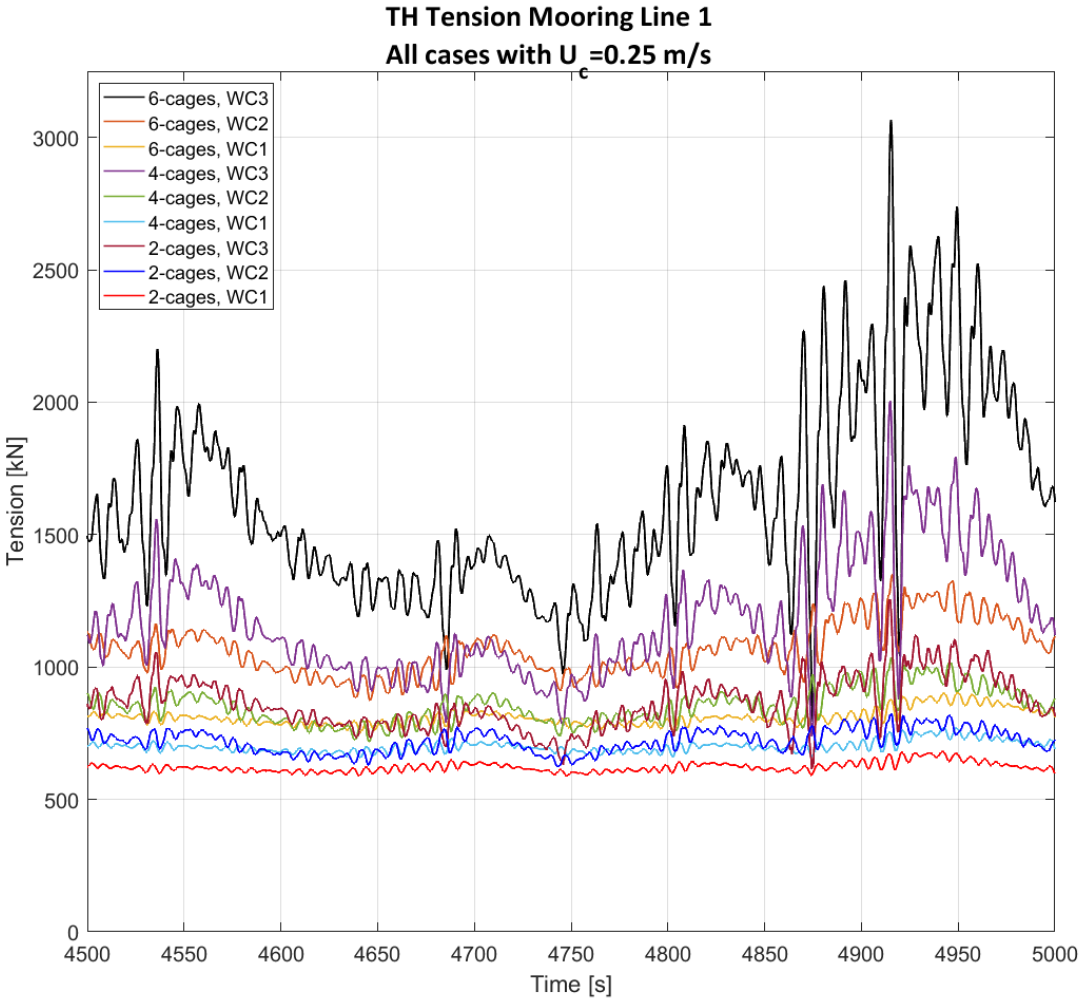

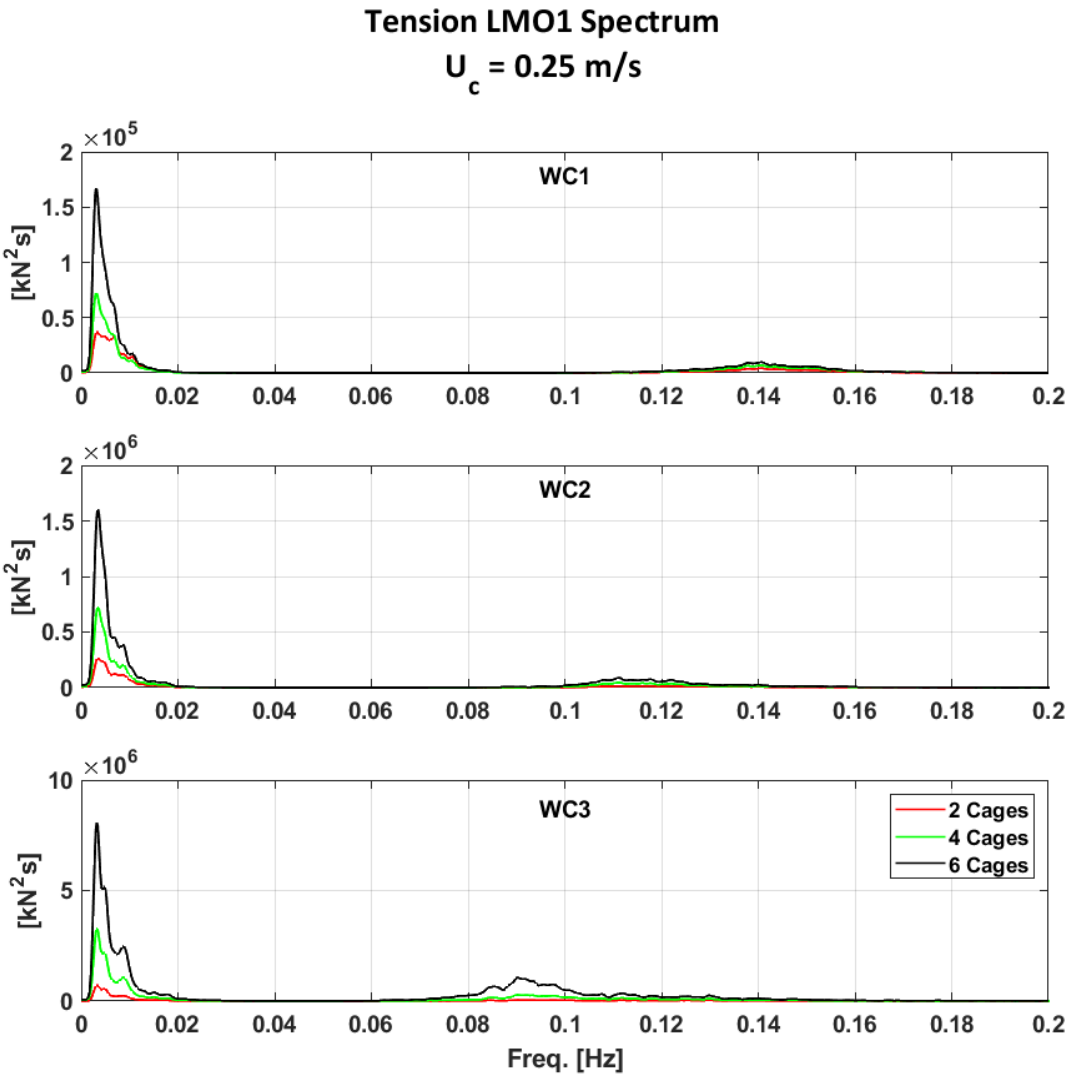
Tension LMO1 Spectrum
U_c = 0.25 m/s
WC1
WC2
WC3
[kN^2 s]
×10^5
×10^6
2 Cages
4 Cages
6 Cages
Freq. [Hz]

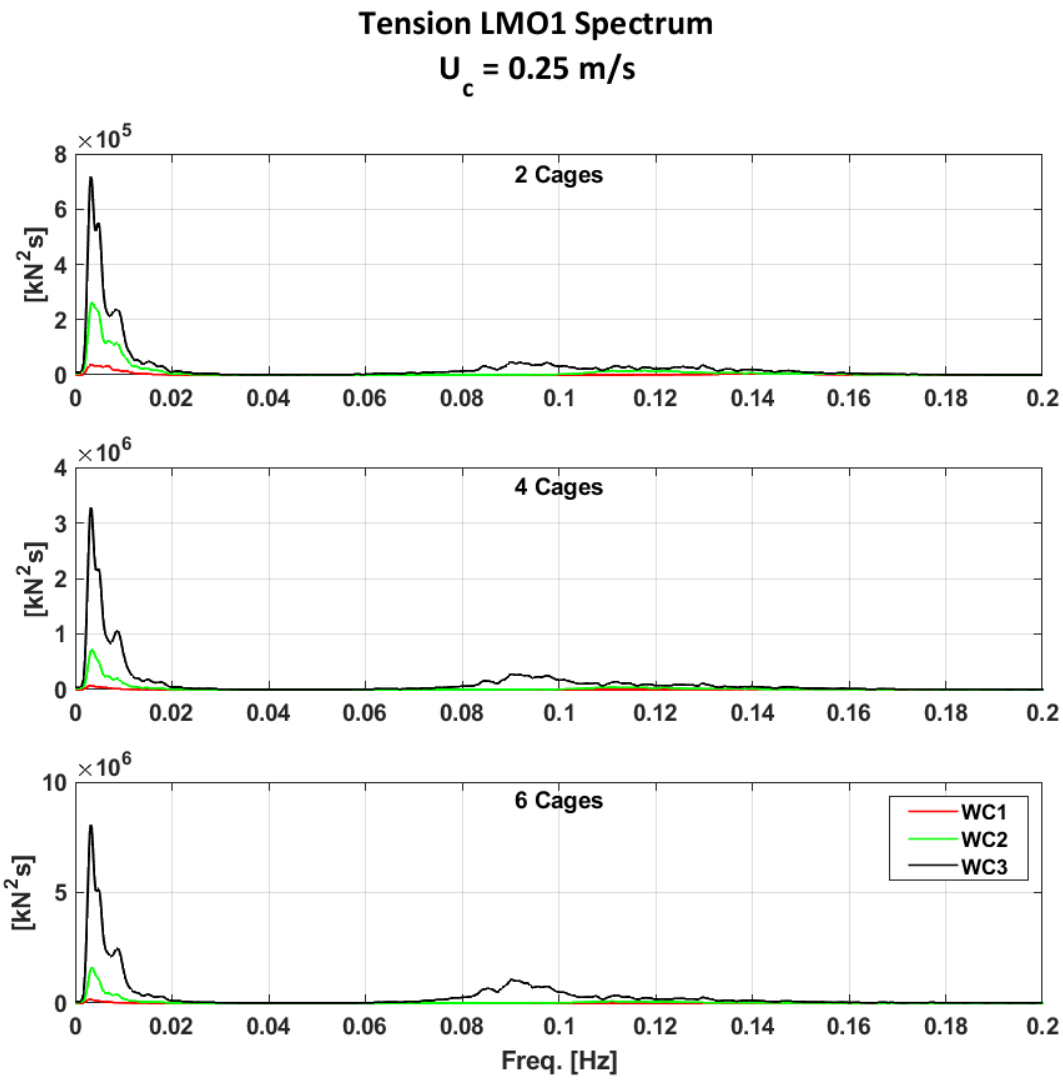
Tension LMO1 Spectrum
U_c = 0.25 m/s
2 Cages
4 Cages
6 Cages
WC1
WC2
WC3
[kN²s]
Freq. [Hz]

Appendix D: Connector axial forces

Case	No. Cages	Wave Cond.	Current Vel.
1*	2 cages	WC1	Uc=0.25 m/s
2*	2 cages	WC2	Uc=0.25 m/s
3*	2 cages	WC3	Uc=0.25 m/s
4*	4 cages	WC1	Uc=0.25 m/s
5*	4 cages	WC2	Uc=0.25 m/s
6*	4 cages	WC3	Uc=0.25 m/s
7*	6 cages	WC1	Uc=0.25 m/s
8*	6 cages	WC2	Uc=0.25 m/s
9*	6 cages	WC3	Uc=0.25 m/s
10*	6 cages	WC3	Uc=0.50 m/s
11*	6 cages	WC3	Uc=0.75 m/s